BASS. XXIII. A new mid-infrared diagnostic for absorption in active galactic nuclei

Pfeifle, R.W.; Ricci, C.; Boorman, P.G.; Stalevski, M.; Asmus, D.; Trakhtenbrot, B.; ... ; Harrison, F.

The Astrophysical Journal Supplement Series, 261:3 (20pp), 2022 July https://doi.org/10.3847/1538-4365/ac5b65

BASS. XXIII. A New Mid-infrared Diagnostic for Absorption in Active Galactic Nuclei

Ryan W. Pfeifle[1], Claudio Ricci[1,2,3], Peter G. Boorman[4,5], Marko Stalevski[6,7], Daniel Asmus[5], Benny Trakhtenbrot[8], Michael J. Koss[9], Daniel Stern[10], Federica Ricci[11], Shobita Satyapal[1], Kohei Ichikawa[12,13], David J. Rosario[14], Turgay Caglar[15], Ezequiel Treister[11], Meredith Powell[16], Kyuseok Oh[17,20,21], C. Megan Urry[18], and Fiona Harrison[19]
[1] Department of Physics & Astronomy, George Mason University, 4400 University Drive, MSN 3F3, Fairfax, VA 22030, USA
[2] Núcleo de Astronomía de la Facultad de Ingeniería, Universidad Diego Portales, Av. Ejército Libertador 441, Santiago, Chile
[3] Kavli Institute for Astronomy and Astrophysics, Peking University, Beijing 100871, People's Republic of China
[4] Astronomical Institute, Academy of Sciences, Boční II 1401, CZ-14131 Prague, Czech Republic
[5] Department of Physics & Astronomy, Faculty of Physical Sciences and Engineering, University of Southampton, Southampton SO17 1BJ, UK
[6] Astronomical Observatory, Volgina 7, 11060 Belgrade, Serbia
[7] Sterrenkundig Observatorium, Universiteit Gent, Krijgslaan 281-S9, Gent, B-9000, Belgium
[8] School of Physics and Astronomy, Tel Aviv University, Tel Aviv 69978, Israel
[9] Eureka Scientific, 2452 Delmer Street, Suite 100, Oakland, CA 94602-3017, USA
[10] Jet Propulsion Laboratory, California Institute of Technology, 4800 Oak Grove Drive, Mail Stop 169-221, Pasadena, CA 91109, USA
[11] Instituto de Astrofísica, Facultad de Física, Pontificia Universidad Catolica de Chile, Casilla 306, Santiago 22, Chile
[12] Frontier Research Institute for Interdisciplinary Sciences, Tohoku University, Sendai 980-8578, Japan
[13] Astronomical Institute, Tohoku University, Aramaki, Aoba-ku, Sendai, Miyagi 980-8578, Japan
[14] School of Mathematics, Statistics and Physics, Newcastle University, Herschel Building, Newcastle upon Tyne, NE1 7RU, UK
[15] Leiden Observatory, PO Box 9513, 2300 RA Leiden, The Netherlands
[16] Kavli Institute of Particle Astrophysics and Cosmology, Stanford University, 452 Lomita Mall, Stanford, CA 94305, USA
[17] Korea Astronomy and Space Science Institute, Daedeokdae-ro 776, Yuseong-gu, Daejeon 34055, Republic of Korea
[18] Department of Physics and Yale Center for Astronomy and Astrophysics, Yale University, 217 Prospect Street, New Haven, CT 06511, USA
[19] Cahill Center for Astronomy and Astrophysics, California Institute of Technology, Pasadena, CA 91125, USA
[20] Department of Astronomy, Kyoto University, Kitashirakawa-Oiwake-cho, Sakyo-ku, Kyoto 606-8502, Japan
Received 2020 August 12; revised 2021 January 25; accepted 2021 February 5; published 2022 July 15

Abstract

In this study, we use the Swift/BAT AGN sample, which has received extensive multiwavelength follow-up analysis as a result of the BAT AGN Spectroscopic Survey, to develop a diagnostic for nuclear obscuration by examining the relationship between the line-of-sight column densities ($N_{\rm H}$), the 2–10 keV to 12 μm luminosity ratio, and WISE mid-infrared colors. We demonstrate that heavily obscured AGNs tend to exhibit both preferentially "redder" mid-infrared colors and lower values of $L_{\rm X,Obs.}/L_{12\ \mu{\rm m}}$ than less obscured AGNs, and we derive expressions relating $N_{\rm H}$ to the $L_{\rm X,Obs.}/L_{12\ \mu{\rm m}}$ and $L_{22\ \mu{\rm m}}/L_{4.6\ \mu{\rm m}}$ luminosity ratios, as well as develop diagnostic criteria using these ratios. Our diagnostic regions yield samples that are $\gtrsim$80% complete and $\gtrsim$60% pure for AGNs with $\log(N_{\rm H}/{\rm cm}^{-2}) \geqslant 24$, as well as $\gtrsim$85% pure for AGNs with $\log(N_{\rm H}/{\rm cm}^{-2}) \gtrsim 23.5$. We find that these diagnostics cannot be used to differentiate between optically star-forming galaxies and active galaxies. Further, mid-IR contributions from host galaxies that dominate the observed 12 μm emission can lead to larger apparent X-ray deficits and redder mid-IR colors than the AGNs would intrinsically exhibit, though this effect helps to better separate less and more obscured AGNs. Finally, we test our diagnostics on two catalogs of AGNs and infrared galaxies, including the XMM-Newton XXL-N field, and we identify several known Compton-thick AGNs, as well as a handful of candidate heavily obscured AGNs based upon our proposed obscuration diagnostics.

Unified Astronomy Thesaurus concepts: Supermassive black holes (1663); Active galactic nuclei (16); Black hole physics (159); X-ray active galactic nuclei (2035); AGN host galaxies (2017)

1. Introduction

Known to reside at the centers of most galaxies (e.g., Ferrarese & Merritt 2000; Kormendy & Ho 2013), supermassive black holes (SMBHs) grow and evolve through periods of activity characterized by the accretion of large quantities of gas. Classically, these active galactic nuclei (AGNs) are categorized based upon the characteristics of their optical spectroscopic emission lines, where the apparent differences between AGNs may be reconciled through a unification scheme involving a dusty obscuring torus (e.g., Antonucci 1993; Urry & Padovani 1995; Netzer 2015; Ramos Almeida & Ricci 2017) for which different inclination angles of the torus correspond to the observation of different AGN classes.

One ubiquitous observational signature of accretion onto SMBHs is X-ray emission, produced very close to the accretion disk (Fabian et al. 2009) due to inverse Compton scattering of optical and ultraviolet (UV) photons from the accretion disk by hot electrons in the corona (Haardt & Maraschi 1991, 1993). In the X-ray band, the line-of-sight gas column density, $N_{\rm H}$, is largely transparent to the 2–10 keV X-ray flux, even up to column densities of a few times 10^{23} cm^{-2}; however, significant attenuation and reprocessing of the 2–10 keV X-ray emission does occur for Compton-thick (CT) AGNs, which possess gas column densities of $\gtrsim 10^{24}$ cm^{-2} (e.g., Lansbury et al. 2014; Bauer et al. 2015; Ricci et al. 2015; Puccetti et al. 2016; LaMassa et al. 2019; Toba et al. 2020). Even at low

[21] JSPS Fellow.

redshift, CT AGNs have proven to be very difficult to find and characterize (Alexander & Hickox 2012) using lower-energy X-ray observatories such as Chandra and XMM-Newton, since the X-ray flux below 10 keV suffers significant photoelectric absorption and Compton scattering. This prevents the detection of some sources, and even those detected have fewer observed photons, which reduces the accuracy of spectral modeling. Important spectral signatures used to characterize the nature of AGNs can be missed without higher-energy X-ray observations (Lansbury et al. 2015; Koss et al. 2016; Ricci et al. 2017a).

CT AGNs are particularly important among the general AGN population, as large fractions of CT AGNs are required to reproduce the observed cosmic X-ray background (CXB; Gilli et al. 2007; Buchner et al. 2015; Ananna et al. 2019). CT AGNs likely represent a significant fraction of the total intrinsic AGN population in the local universe (∼20%, Burlon et al. 2011; ∼27%, Ricci et al. 2015), with the most recent SMBH synthesis model developed by Ananna et al. (2019) suggesting that CT AGNs represent $50\% \pm 9\%$ and $56\% \pm 7\%$ of the total intrinsic AGN population up to both $z \sim 0.1$ and 1.0, respectively,[22] and recent works by Carroll et al. (2021, 2022) have revealed large populations of previously unaccounted CT AGNs, in apparent agreement with the large fractions of CT AGNs predicted by Ananna et al. (2019). Furthermore, questions remain regarding the exact nature of the obscuring structure and how it relates to, for example, the host environment; some CT AGNs could represent the evolutionary phase predicted to occur as a result of galaxy mergers (e.g., Hopkins et al. 2008; Kocevski et al. 2015; Ricci et al. 2017b; Blecha et al. 2018). Identifying further cases of CT AGNs is crucial for providing a full census of accreting SMBHs and placing constraints on the CXB and evolutionary and unification models.

The UV radiation from the accretion disk is also reprocessed by the obscuring dusty torus, wherein the radiation is scattered and absorbed by the dust grains and reemitted thermally with a peak usually at mid-infrared (mid-IR) wavelengths. While the classically accepted origin of the mid-IR emission is the dusty torus itself, recent high angular resolution IR observations of AGNs suggest that the mid-IR emission is in fact dominated by a dusty polar outflow rather than the torus itself (e.g., Hönig et al. 2012, 2013; Tristram et al. 2014; Asmus et al. 2016; Hönig & Kishimoto 2017; Stalevski et al. 2018; Hönig 2019). Other recent studies (Baron & Netzer 2019a, 2019b) have actually attributed mid-IR emission to dusty outflows located on the order of tens to hundreds of parsecs from the centers of the galaxies.

A correlation between the intrinsic (unabsorbed) hard X-ray 2–10 keV luminosity (L_X) and mid-IR luminosity (L_{MIR}) of AGNs was reported as early as Elvis et al. (1978). Universally, studies find no difference (<0.3 dex) in the ratios of L_X to L_{MIR} between type 1 and 2 AGNs (Lutz et al. 2004; Levenson et al. 2009; Gandhi et al. 2009; Ichikawa et al. 2012; Mateos et al. 2015; Asmus et al. 2015), and this ratio is also insensitive to the neutral gas column density along the line of sight (Gandhi et al. 2009; Mateos et al. 2015; Asmus et al. 2015), even in the case of CT AGNs after correcting the X-rays for absorption (Gandhi et al. 2009). Many previous studies have also pointed out that this relation can serve as a useful tool to select obscured, particularly CT, AGNs because CT AGNs tend to exhibit severe deficits in their absorbed X-ray emission when compared to their mid-IR emission; thus, CT AGNs fall significantly off of the L_X-to-L_{MIR} relation (Alexander et al. 2008; Goulding et al. 2011; Georgantopoulos et al. 2011; Rovilos et al. 2014; Asmus et al. 2015). Moreover, Asmus et al. (2015) also demonstrated that the ratio of L_X/L_{MIR} can be used to predict column densities for significantly obscured objects, deriving an equation that relates L_X/L_{MIR} to $\log(N_H/\mathrm{cm}^{-2})$ for $\log(N_H/\mathrm{cm}^{-2}) > 22.8$.

It is important to gather large samples of powerful AGNs across a range of column densities to test the utility of the X-ray–to–mid-IR relation as a tracer of nuclear obscuration. Hard X-ray selection provides one of the least biased methods of identifying powerful AGNs, as hard X-ray emission is largely unaffected by the line-of-sight obscuration for column densities $<10^{24}$ cm^{-2} (see Figure 1 from Ricci et al. 2015). The Swift/BAT ultrahard X-ray (14–195 keV) all-sky survey has dramatically increased the number of known hard X-ray extragalactic sources (Baumgartner et al. 2013; Oh et al. 2018) and has therefore been the focus of a large multi-wavelength follow-up campaign (the BAT AGN Spectroscopic Survey, BASS[23]) designed to characterize the most powerful AGNs in the local universe (Koss et al. 2017; Ricci et al. 2017a; Lamperti et al. 2017). A second release of optical spectroscopy (BASS DR2) is also publicly available (Koss et al. 2022; Oh et al. 2022). Ricci et al. (2017a) presented a detailed X-ray analysis of 838 ultrahard X-ray–detected Swift/BAT AGNs, providing constraints on column densities (N_H), as well as the absorbed (observed) and unabsorbed 2–10 keV luminosities, while Ichikawa et al. (2017) provided mid-to-far-IR photometric data and corresponding IR luminosities for the 604 mid-IR-detected Swift/BAT AGNs. These two catalogs provide precisely the information needed to test the relationship between the absorbed hard X-ray and mid-IR emission with respect to the line-of-sight obscuration in AGNs.

In this paper, we present a new diagnostic for absorption in AGNs that combines the power of the known $L_X/L_{12\,\mu m}$ correlation with Wide-field Infrared Survey Explorer (WISE) mid-IR colors. Using multiwavelength catalogs available for the Swift/BAT hard X-ray–selected sample of AGNs, we show that this diagnostic reliably identifies the most obscured AGNs, at least for nearby X-ray-bright AGNs. Our proposed diagnostics could prove valuable in the search for obscured AGNs in the ongoing eROSITA survey (Predehl et al. 2010; Merloni et al. 2012). In Section 2, we describe our sample. In Section 3, we describe the analysis of the sample and propose our new absorption diagnostics, as well as develop expressions that constrain column densities. In Section 4, we explore the emission ratios of optically selected star-forming galaxies, compare our diagnostics for obscuration to other recent studies, and apply our diagnostics to the XMM-Newton XXL North (XXL-N) field (Pierre et al. 2016, 2017). In Section 5, we detail our conclusions. Throughout this manuscript, we assume the following cosmological values: $H_0 = 70$ km s^{-1} Mpc^{-1}, $\Omega_M = 0.3$, and $\Omega_\Lambda = 0.7$. All luminosities quoted in this work are given in units of ergs per second.

[22] Though many previous synthesis models predicted lower intrinsic fractions of CT AGNs than this, including but not limited to Gilli et al. (2007), Treister et al. (2009), Akylas et al. (2012), and Ueda et al. (2014).

[23] https://www.bass-survey.com/

2. Sample Construction

We selected our sample from the 70 month Swift/BAT X-ray properties catalog (Ricci et al. 2017a), which details the broadband 0.3–150 keV X-ray spectral properties of the 838 AGNs detected in the ultrahard X-ray 14–195 keV band by Swift/BAT and reported in the 70 month source catalog (Baumgartner et al. 2013). We matched this catalog to the 70 month Swift/BAT IR catalog of Ichikawa et al. (2017), which provides the complete near-to-far-IR photometry for 604 Swift/BAT nonbeamed AGNs at high Galactic latitudes ($|b| > 10°$). We refer the reader to Ricci et al. (2017a) and Ichikawa et al. (2017) for further details on the construction of these catalogs. These catalogs yielded a parent sample of 604 nonbeamed AGNs; any systems flagged as beamed in the Ricci et al. (2017a) catalog were removed during the matching process.

In order to conduct our analysis, we required X-ray and mid-IR detections in all four WISE bands for the AGNs in our sample, which excluded another 78 AGNs from the final sample.[24] We adopted the hard X-ray 2–10 keV luminosities (observed, uncorrected for intrinsic absorption) from Ricci et al. (2017a) and the IR luminosities in all four WISE bands (3.6, 4.6, 12, and 22 μm) from Ichikawa et al. (2017), which are not corrected for any host galaxy contributions. We further limited the sample to $z < 0.1$ AGNs to avoid redshift effects; this redshift cut removed another 70 AGNs from the sample. The Ricci et al. (2017a) catalog includes independent estimates of $N_{\rm H}$ from a torus model in the event that the column density found with the phenomenological model was $\geqslant 10^{24}$ cm^{-2}. In these cases, we instead use the column density inferred from the torus model, because torus models more accurately account for the 2–10 keV emission of CT AGNs.

Following the matching of the catalogs and the application of the above requirements, the final sample was composed of 456 nearby, nonbeamed AGNs with a median redshift of $z \simeq 0.032$ and mid-IR luminosities in the range $1.6 \times 10^{39} \leqslant L_{12\ \mu{\rm m}}/{\rm erg\ s^{-1}} \leqslant 8.5 \times 10^{44}$.

3. Data Analysis

Comparing the observed X-ray 2–10 keV luminosities ($L_{\rm X,Obs.}$) to the 12 μm luminosities ($L_{12\ \mu{\rm m}}$), we see in Figure 1 that unobscured Swift/BAT AGNs tend to follow the relation between the intrinsic (unabsorbed) 2–10 X-ray and nuclear 12 μm luminosities (dashed black line) established by Asmus et al. (2015), whereas obscured AGNs appear X-ray suppressed when compared to $L_{12\ \mu{\rm m}}$. This decrease in $L_{\rm X,Obs.}$ compared to $L_{12\ \mu{\rm m}}$ with increasing column density is expected, of course, since the X-ray emission will suffer greater attenuation than the mid-IR emission, and we color code the data in Figure 1 according to the column densities adopted in Section 2. As a population, CT AGNs are generally the furthest offset from the Asmus et al. (2015) relation, exhibiting luminosity ratios of $\log(L_{\rm X,Obs.}/L_{12\ \mu{\rm m}}) < -1.3$ (this was previously discussed in, e.g., Alexander et al. 2008); we plot this ratio between $\log(L_{\rm X,Obs.})$ and $\log(L_{12\ \mu{\rm m}})$ as a dotted black line in Figure 1. As has been done in previous works (e.g., Alexander et al. 2008; Goulding et al. 2011; Asmus et al. 2015), we can use this ratio between $L_{\rm X,Obs.}$ and $L_{12\ \mu{\rm m}}$ as a diagnostic tool to differentiate between less and heavily obscured CT AGNs.

[24] While detected in the WISE W1 [3.4 μm] and W2 [4.6 μm] bands, 67 AGNs did not satisfy the WISE data quality cuts established in Section 2.2.1 of Ichikawa et al. (2017). A further 11 AGNs did not possess detections at either 12 or 22 μm. All AGNs within the parent sample of 604 AGNs possessed 2–10 keV X-ray detections.

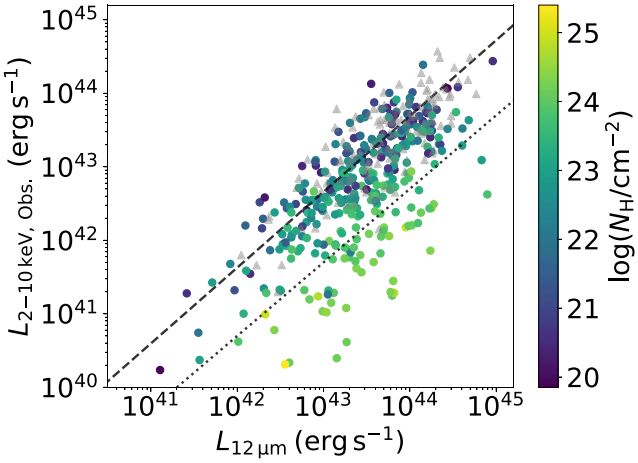

Figure 1. Observed 2–10 keV X-ray vs. 12 μm luminosities. We color code the data points using the derived column density from the Ricci et al. (2017a) catalog, where the color map is denoted on the auxiliary axis. Gray triangles denote AGNs with $N_{\rm H}$ upper limits of $\log(N_{\rm H}/{\rm cm^{-2}}) \leqslant 20.0$. When comparing the 2–10 keV X-ray luminosity to the 12 μm luminosity for our sample of 456 Swift/BAT AGNs, we see a general decrease in the X-ray–to–mid-IR ratio with increasing column density, as expected. The relation between the AGN intrinsic 2–10 keV luminosity (corrected for absorption) and the nuclear 12 μm luminosity derived by Asmus et al. (2015) is represented by a dashed black line, whereas we plot the logarithmic ratio of $\log(L_{\rm X,Obs.}/L_{12\ \mu{\rm m}}) = -1.3$ with a black dotted line. Most heavily obscured (CT) AGNs exhibit luminosity ratios $\log(L_{\rm X,Obs.}/L_{12\ \mu{\rm m}}) < -1.3$.

Ratios of two mid-IR luminosities, sufficiently separated in wavelength, could exhibit the same trend as observed for the $L_{\rm X,Obs.}/L_{12\ \mu{\rm m}}$ ratio, in that the shorter-wavelength mid-IR emission could appear suppressed compared to the longer-wavelength emission due to the obscuring material surrounding the AGN. We test a new diagnostic tool based on the ratio of the WISE 22 to 4.6 μm luminosity ($L_{22\ \mu{\rm m}}/L_{4.6\ \mu{\rm m}}$) in Figure 2, and we find that the logarithmic ratio increases with column density, with the most significant increase in the WISE ratio corresponding to the highest column densities (although with significant scatter). For example, we find a mean luminosity ratio and 1σ uncertainty of $\log(L_{22\ \mu{\rm m}}/L_{4.6\ \mu{\rm m}}) = 0.50 \pm 0.32$ for AGNs with $\log(N_{\rm H}/{\rm cm^{-2}}) \geqslant 24$, whereas we find a mean ratio and 1σ uncertainty of $\log(L_{22\ \mu{\rm m}}/L_{4.6\ \mu{\rm m}}) = 0.06 \pm 0.25$ for unobscured AGNs with column densities $\log(N_{\rm H}/{\rm cm^{-2}}) < 22$. This suggests that WISE colors can also be used as a diagnostic tool for identifying heavily absorbed AGNs.

We combine the $L_{\rm X,Obs.}/L_{12\ \mu{\rm m}}$ and $L_{22\ \mu{\rm m}}/L_{4.6\ \mu{\rm m}}$ ratio diagnostics in Figure 3, plotting the two diagnostic ratios against one another in panel (a) and color coding the data points by column density on the auxiliary axis. As the column density increases, the AGNs tend to exhibit lower values of $L_{\rm X,Obs.}/L_{12\ \mu{\rm m}}$ and higher values of $L_{22\ \mu{\rm m}}/L_{4.6\ \mu{\rm m}}$; thus, we find that the most heavily obscured AGNs predominantly occupy the lower right portion of the parameter space (i.e., the largest X-ray deficits and highest $L_{22\ \mu{\rm m}}/L_{4.6\ \mu{\rm m}}$ ratios). In Figure 3(b), we show this same result after binning the data by $L_{22\ \mu{\rm m}}/L_{4.6\ \mu{\rm m}}$. In panel (c), we bin by $L_{22\ \mu{\rm m}}/L_{4.6\ \mu{\rm m}}$ and examine the scatter in the column density by bin; we notice a positive correlation between the column density and the mid-IR luminosity ratio. All solid error bars in panels (b) and (c) represent the standard error of the mean, while dashed error bars represent the standard deviation computed for

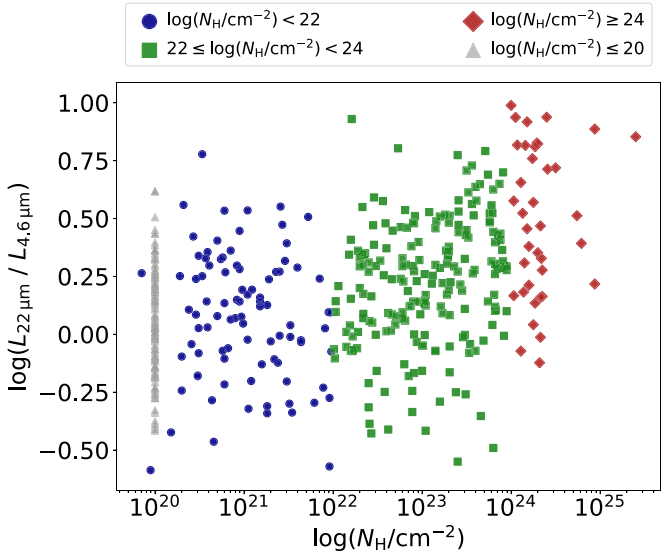

Figure 2. Ratio of the 22 and 4.6 μm WISE luminosities as a function of column density (reported in Ricci et al. 2017a). We differentiate between unobscured (blue circles), Compton-thin (green squares), and CT (red diamonds) AGNs, as denoted in the legend. Gray triangles denote AGNs with $N_{\rm H}$ upper limits of $\log(N_{\rm H}/{\rm cm}^{-2}) \leqslant 20.0$. While there is a large amount of scatter, there is a general upturn in the luminosity ratio at the highest column densities, beginning at $\sim$5–8 $\times$ 10^{23} cm^{-2}.

the respective bin. Considering these three panels together, we may define a parameter space using the $L_{\rm X,Obs.}/L_{12\ \mu{\rm m}}$ and $L_{22\ \mu{\rm m}}/L_{4.6\ \mu{\rm m}}$ luminosity ratios, which could be used to identify the most heavily absorbed AGNs. We repeated this analysis for an alternative WISE luminosity ratio of $L_{12\ \mu{\rm m}}/L_{4.6\ \mu{\rm m}}$ and found very similar results (see Figure 4). We explored several AGN selection methods to potentially mitigate or at least account for the scatter observed, which we discuss in the Appendix. Ultimately, we did not apply any selection criteria to our sample of Swift/BAT AGNs during the analysis described below. Of important note, however, is the interesting result that the correlation between the mid-IR color and $N_{\rm H}$ holds true for both WISE (selected via W1 − W2 > 0.8; Stern et al. 2012) and non-WISE AGNs.

3.1. A Relation for N_H as a Function of $L_{X,Obs.}/L_{12\ \mu m}$

Since the $L_{\rm X,Obs.}/L_{12\ \mu{\rm m}}$ ratio is known to correlate with the obscuring column (e.g., Ichikawa et al. 2012; Asmus et al. 2015; Yan et al. 2019), we derived an expression to describe this relationship using the Swift/BAT sample studied here. Note that, in contrast to Asmus et al. (2015; see Section 4.2 for further details), we do not exclude sources with $\log(N_{\rm H}/{\rm cm}^{-2}) < 22.8$ from the fitting process.

For our fitting process, we incorporate the luminosity ratios and associated uncertainties. We pull the uncertainties in the mid-IR fluxes from Ichikawa et al. (2017, 2019); while the uncertainties in the observed X-ray luminosities were not available in the Ricci et al. (2017a) catalog, we conservatively adopt uncertainties of $\log(L_{\rm X,Obs.}) = \pm 0.1$ for AGNs with $\log(N_{\rm H}/{\rm cm}^{-2}) < 24$ and $\log(L_{\rm X,Obs.}) = \pm 0.3$ for AGNs with $\log(N_{\rm H}/{\rm cm}^{-2}) \geqslant 24$. In order to take into account the asymmetric uncertainties associated with $\log(N_{\rm H}/{\rm cm}^{-2})$ and $\log(L_{\rm X,Obs.}/L_{12\ \mu{\rm m}})$, we employed the following Monte Carlo (MC) fitting routine.

1. *Bootstrap*. To fully account for the effect of outliers, we generated a new data set as a sample of the original, allowing repeats.

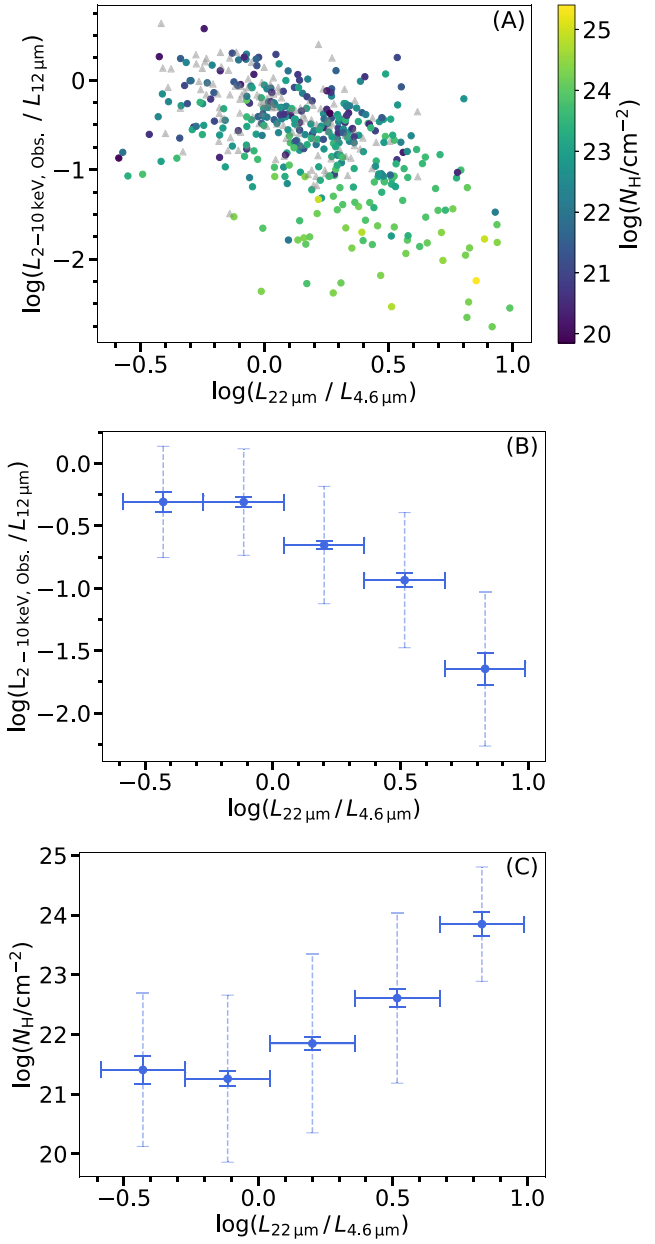

Figure 3. Logarithmic $L_{\rm X,Obs.}/L_{12\ \mu{\rm m}}$ and $L_{22\ \mu{\rm m}}/L_{4.6\ \mu{\rm m}}$ luminosity ratios (panel (a)), with each point color coded to indicate the column density (as indicated by the auxiliary axis). Sources with $N_{\rm H}$ upper limits of $\log(N_{\rm H}/{\rm cm}^{-2}) < 20.0$ are denoted with gray triangles. Binning by the $L_{22\ \mu{\rm m}}/L_{4.6\ \mu{\rm m}}$ luminosity ratio (panel (b)), we see a general trend of decreasing X-ray–to–mid-IR ratio with increasing values of the $L_{22\ \mu{\rm m}}/L_{4.6\ \mu{\rm m}}$ ratio. Binning by the $L_{22\ \mu{\rm m}}/L_{4.6\ \mu{\rm m}}$ luminosity ratio and comparing it to the column density (panel (c)), we see a general trend of increasing WISE luminosity ratios with increasing column density. Solid error bars in panels (b) and (c) represent the standard error of the mean, while dashed error bars represent the standard deviation computed for the respective bin.

2. *MC*. For each point in the bootstrapped data set, we generate a new point given the uncertainties in $\log(N_{\rm H}/{\rm cm}^{-2})$ and $\log(L_{\rm X,Obs.}/L_{12\ \mu{\rm m}})$. We incorporate asymmetric error bars by randomly drawing from a Gaussian distribution separately for the negative and positive error bars. For upper limits in $\log(N_{\rm H})$,[25] we generate a new point using a uniform distribution from the

[25] Note that there are no limits for $\log(L_{\rm X,Obs.}/L_{12\ \mu{\rm m}})$.

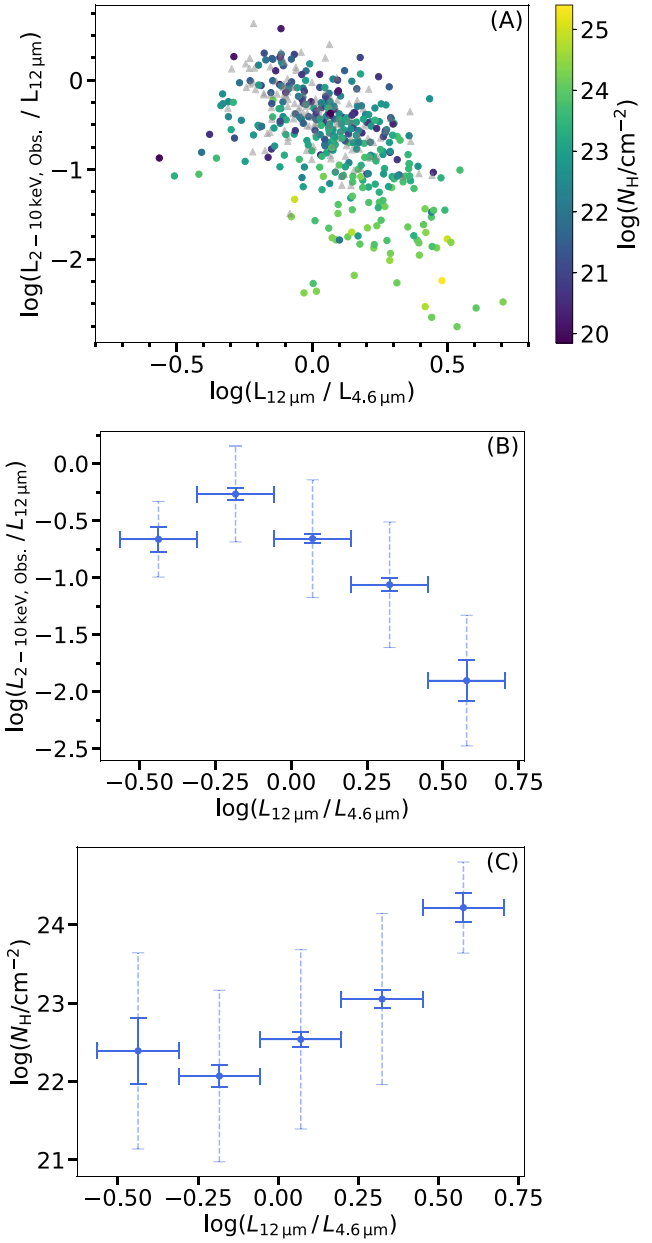

Figure 4. In an identical fashion to that shown in Figure 3, we show the logarithmic $L_{\mathrm{X,Obs.}}/L_{12\ \mu\mathrm{m}}$ and $L_{12\ \mu\mathrm{m}}/L_{4.6\ \mu\mathrm{m}}$ luminosity ratios (panel (a)), with the column density given on the auxiliary axis. We find very similar results to those shown in Figure 3 when binning and comparing the $L_{\mathrm{X,Obs.}}/L_{12\ \mu\mathrm{m}}$ and $L_{12\ \mu\mathrm{m}}/L_{4.6\ \mu\mathrm{m}}$ luminosity ratios (panel (b)) and the $L_{12\ \mu\mathrm{m}}/L_{4.6\ \mu\mathrm{m}}$ ratio and N_{H} (panel (c)).

limit to an arbitrarily small $\log(N_{\mathrm{H}}/\mathrm{cm}^{-2})$ value below it. After experimenting with a number of different values, each giving similar results, we settled for a lower bound of $\log(N_{\mathrm{H}}/\mathrm{cm}^{-2}) = 19$, which is only marginally lower than the smallest $\log(N_{\mathrm{H}}/\mathrm{cm}^{-2})$ value through the Milky Way according to the maps by Kalberla et al. (2005).

3. *Orthogonal distance regression*. We fit each MC-bootstrapped data set with a function of the form $y = a \cdot 10^{b\cdot(x-20)} + c$ using orthogonal distance regression (from the Python SCIPY package ODR; Boggs & Rogers et al. 1990; Virtanen et al. 2020). This ensures we account for minimization in both variables during the fitting procedure.

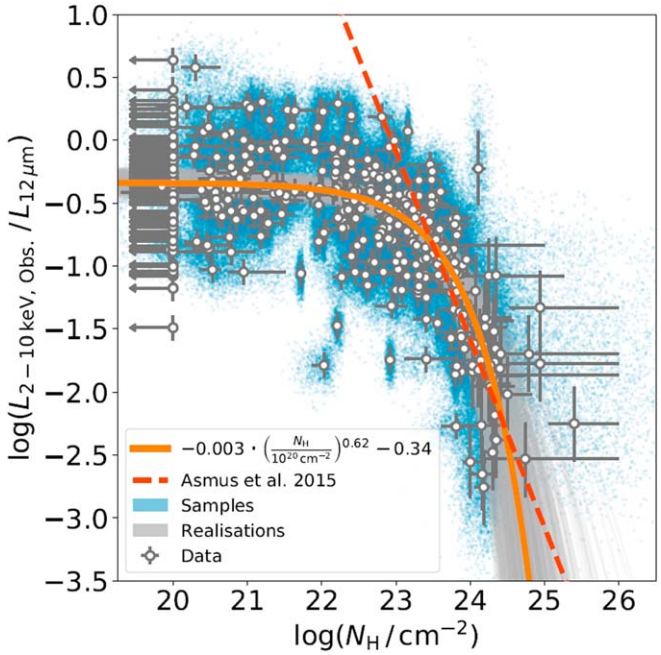

Figure 5. Relation for the column density vs. $\log(L_{\mathrm{X,Obs.}}/L_{12\ \mu\mathrm{m}})$ for the Swift/BAT sample (white circles). New data samples simulated during the MC fitting routine are displayed as blue dots. The best-fit trend line (orange line, given by Equation (1)) represents the median of 1000 realizations (gray lines) obtained through orthogonal distance regression during the MC fitting process (see Section 3.1). The best-fit relation from Asmus et al. (2015) is shown as a red dashed line.

4. *Parameter estimation*. Steps 1–3 were performed many times, giving a distribution for the parameters a, b, and c. For each parameter, we report the 50th percentile and uncertainties derived from the 84th and 16th percentiles.

The relationship between $L_{\mathrm{X,Obs.}}/L_{12\ \mu\mathrm{m}}$ and N_{H} can be expressed as

$$\log(L_{\mathrm{X,Obs.}}/L_{12\ \mu\mathrm{m}}) = (-0.34^{+0.06}_{-0.06}) + (-0.003^{+0.002}_{-0.005}) \times (N_{\mathrm{H}}/10^{20}\ \mathrm{cm}^{-2})^{(0.62^{+0.13}_{-0.12})}. \quad (1)$$

We plot the Swift/BAT sample and Equation (1) (orange line) in Figure 5. To visualize the uncertainty in this relation, we show the 1000 realizations of the best fit as gray lines.

We attempted to fit directly for $\log(N_{\mathrm{H}})$ as a function of $\log(L_{\mathrm{X,Obs.}}/L_{12\ \mu\mathrm{m}})$, but the fitting routine could not successfully converge on a reasonable fit to the data. Instead, we chose to invert Equation (1) to recover the obscuring column density as a function of the X-ray–to–mid-IR luminosity ratio:

$$\log(N_{\mathrm{H}}/\mathrm{cm}^{-2}) = 20 + (1.61^{+0.33}_{-0.31}) \times \log\left(\left|\frac{\log\left(\frac{L_{\mathrm{X,Obs.}}}{L_{12\ \mu\mathrm{m}}}\right) + (0.34^{+0.06}_{-0.06})}{(-0.003^{+0.002}_{-0.005})}\right|\right). \quad (2)$$

To better quantify the uncertainty in $\log(N_{\mathrm{H}}/\mathrm{cm}^{-2})$ associated with this relation, we tabulated values of $\log(N_{\mathrm{H}})$ and the uncertainty for specific values of $\log(L_{\mathrm{X,Obs.}}/L_{12\ \mu\mathrm{m}})$, as shown in Table 1. Using the parameter distributions calculated during the MC fitting routine, we derived a distribution of $\log(N_{\mathrm{H}}/\mathrm{cm}^{-2})$ values using an expression of the form shown in Equation (2) (inverted from Equation (1)) and use the 16th, 50th, and 84th

Table 1
$\log(N_{\rm H}/{\rm cm}^{-2})$ Derived from Equations (2) and (9)

$\log(L_{\rm X,Obs.}/L_{12\ \mu{\rm m}})$ (1)	$\log(N_{\rm H}/{\rm cm}^{-2})$ (This Work) (2)	$\log(N_{\rm H}/{\rm cm}^{-2})$ (Asmus et al. 2015) (3)
−0.3	$21.8^{+0.7}_{-1.0}$	23.1 ± 0.1
−0.5	$22.7^{+0.2}_{-0.3}$	23.3 ± 0.1
−0.75	$23.4^{+0.1}_{-0.1}$	23.4 ± 0.2
−1.0	$23.7^{+0.1}_{-0.1}$	23.6 ± 0.2
−1.3	$24.0^{+0.2}_{-0.1}$	23.8 ± 0.2
−1.5	$24.1^{+0.2}_{-0.1}$	23.9 ± 0.3
−2.0	$24.4^{+0.2}_{-0.2}$	24.3 ± 0.3
−2.5	$24.5^{+0.3}_{-0.2}$	24.6 ± 0.4
−3.0	$24.7^{+0.3}_{-0.2}$	25.0 ± 0.4

Note. Column densities as a function of $\log(L_{\rm X,Obs.}/L_{12\ \mu{\rm m}})$. Column 1: logarithmic ratio of the 2–10 keV to 12 μm luminosities. Equation (2) is insensitive to ratios of $\log(L_{\rm X,Obs.}/L_{12\ \mu{\rm m}}) > -0.3$, which are largely exhibited by AGNs with $\log(N_{\rm H}/{\rm cm}^{-2}) < 23$. Column 2: column density and associated error, derived by Equation (2). The parameter distributions found during the MC fitting process described in Section 3.1 were read into an inverted expression of the form in Equation (2), from which we retrieved the median column density and upper and lower bounds using the 16th, 50th, and 84th percentiles of the resulting $\log(N_{\rm H}/{\rm cm}^{-2})$ distribution. Column 3: column density derived using Equation (6) from Asmus et al. (2015).

percentiles of the distribution to list the median column density and associated uncertainty for each chosen value of $\log(L_{\rm X,Obs.}/L_{12\ \mu{\rm m}})$. While strictly empirical, Equations (1) and (2) reproduce the observed trend of decreasing values of $\log(L_{\rm X,Obs.}/L_{12\ \mu{\rm m}})$ with increasing column density. We do note that this relation is largely insensitive to ratios of $\log(L_{\rm X,Obs.}/L_{12\ \mu{\rm m}}) > -0.3$, with the relation appearing nearly flat for column densities of $\log(N_{\rm H}/{\rm cm}^{-2}) < 22.5$. Equations (1) and (2) are most effective for obscured AGNs with column densities of $\log(N_{\rm H}/{\rm cm}^{-2}) \geqslant 22.5$, and readers should keep this in mind when using these expressions to derive estimates for column densities.

We compare these results to those found in Asmus et al. (2015) in Section 4.2, and we plot the best-fit relation for $\log(N_{\rm H})$ versus $\log(L_{\rm X,Obs.}L_{12\ \mu{\rm m}})$ found by Asmus et al. (2015) in Figure 5.

3.2. Relation between N_H and the Mid-IR Colors

Given the correlation between $L_{22\ \mu{\rm m}}/L_{4.6\ \mu{\rm m}}$ and $N_{\rm H}$, as shown in Figure 3, we followed the same fitting procedure as discussed above to develop an expression relating the mid-IR luminosity ratio and $N_{\rm H}$. The equation relating these properties can be expressed as

$$\log(L_{22\ \mu{\rm m}}/L_{4.6\ \mu{\rm m}}) = (0.04^{+0.02}_{-0.02}) + 0.03^{+0.02}_{-0.02}) \times (N_{\rm H}/10^{20}\ {\rm cm}^{-2})^{(0.26^{+0.13}_{-0.07})}. \quad (3)$$

In Figure 6, we plot the Swift/BAT sample and the best-fitting trend line (orange line) along with 1000 realizations of the best fit found during the fitting procedure (shown as gray lines).

As mentioned in Section 3.1, we attempted to fit directly for $N_{\rm H}$ as a function of $L_{\rm X,Obs.}/L_{12\ \mu{\rm m}}$, but the fitting routine could not successfully converge on a reasonable line of best fit. We therefore simply invert Equation (3) like before to recover the

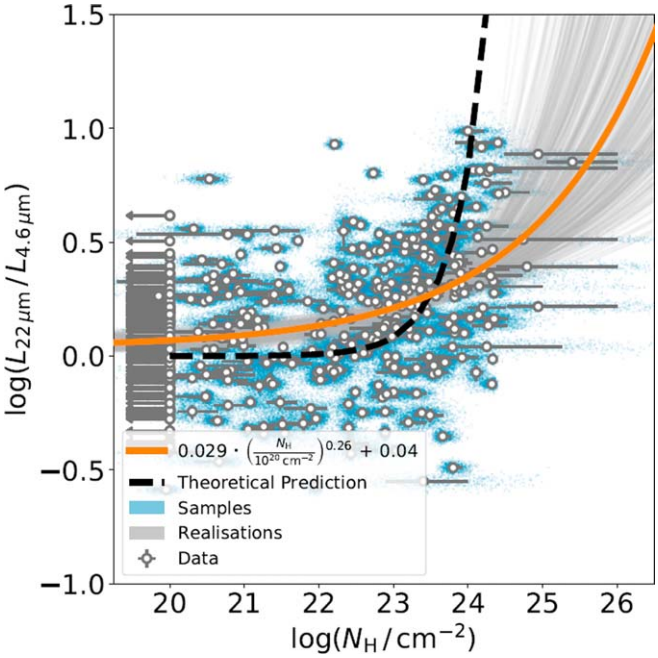

Figure 6. Relation for column density vs. $\log(L_{22\ \mu{\rm m}}/L_{4.6\ \mu{\rm m}})$ for the Swift/BAT sample (white circles). The fitting process for this relation is identical to that in Figure 5. The best-fit trend line (orange line, given by Equation (1)) represents the median of 1000 realizations (gray lines) obtained during the MC fitting process. The black dashed line represents a theoretical prediction for a simple model consisting of monochromatic radiation passing through a homogeneous screen of dust (see Section 4.1.)

column density as a function of the mid-IR luminosity ratio:

$$\log(N_{\rm H}/{\rm cm}^{-2}) = 20 + (3.86^{+1.94}_{-1.00}) \times \log\left(\left|\frac{\log\left(\frac{L_{22\ \mu{\rm m}}}{L_{4.6\ \mu{\rm m}}}\right) - (0.04^{+0.02}_{-0.02})}{(0.03^{+0.02}_{-0.02})}\right|\right). \quad (4)$$

In an identical fashion to the calculations in Section 3.1, we tabulated values of $\log(N_{\rm H}/{\rm cm}^{-2})$ and the associated uncertainties for specific values of $\log(L_{22\ \mu{\rm m}}/L_{4.6\ \mu{\rm m}})$ in Table 2. Equation (4) is not sensitive to values of $\log(L_{22\ \mu{\rm m}}/L_{4.6\ \mu{\rm m}}) < 0$, and, as in the case of Equation (2), readers should use this relation cautiously and bear in mind that it is really only effective for obscured AGNs with $\log(N_{\rm H}/{\rm cm}^{-2}) \geqslant 22.5$.

3.3. Diagnostic Regions for Heavily Absorbed AGNs

The correlations between $L_{\rm X,Obs.}/L_{12\ \mu{\rm m}}$, $L_{22\ \mu{\rm m}}/L_{4.6\ \mu{\rm m}}$, and $N_{\rm H}$ discussed above suggest that these relationships may be combined to help differentiate between Swift/BAT AGNs according to the levels of obscuration. We probed this potential diagnostic for heavily absorbed AGNs by plotting $L_{22\ \mu{\rm m}}/L_{4.6\ \mu{\rm m}}$ versus $L_{\rm X,Obs.}/L_{12\ \mu{\rm m}}$ and binning the full sample by absorbing column, as shown in Figure 7. The sample was divided into four bins in obscuration corresponding to

1. unobscured [$\log(N_{\rm H}/{\rm cm}^{-2}) < 22$; panel (a)];
2. Compton-thin "lightly obscured" [$22 \leqslant \log(N_{\rm H}/{\rm cm}^{-2}) < 23$; panel (b)];
3. Compton-thin "moderately obscured" [$23 \leqslant \log(N_{\rm H}/{\rm cm}^{-2}) < 24$; panel (c)]; and

Table 2
$\log(N_H/cm^{-2})$ Derived from Equation (4)

$\log(L_{22\ \mu m}/L_{4.6\ \mu m})$ (1)	$\log(N_H/cm^{-2})$ (2)
0.0	$20.6^{+1.4}_{-2.2}$
0.1	$21.3^{+0.6}_{-0.8}$
0.2	$22.9^{+0.2}_{-0.3}$
0.25	$23.4^{+0.2}_{-0.2}$
0.3	$23.7^{+0.2}_{-0.2}$
0.4	$24.2^{+0.4}_{-0.3}$
0.5	$24.7^{+0.5}_{-0.4}$
0.75	$25.4^{+0.7}_{-0.6}$
1.0	$25.9^{+0.9}_{-0.8}$

Note. Column densities as a function of $\log(L_{22\ \mu m}/L_{4.6\ \mu m})$. Column 1: logarithmic ratio of the 22 to 4.6 μm luminosities. Equation (2) is insensitive to ratios of $\log(L_{22\ \mu m}/L_{4.6\ \mu m}) > 0$. Column 2: column density and associated error, derived by Equation (4). The median value and associated uncertainties were derived in an identical fashion to that described in Table 1.

4. "heavily obscured" to CT [$\log(N_H/cm^{-2}) \geqslant 24$; panel (d)].

We also split the two Compton-thin bins into two sub-bins, each in increments of $\log(N_H/cm^{-2}) = 0.5$, as summarized in Table 3.

Contours were computed for each bin and/or sub-bin and in each case are designed to encompass ~68% of the population of each respective bin. The binned subplots shown in Figure 7 demonstrate much more clearly that, in general, the heavily obscured sources (panel (d)) tend to occupy a separate region of space than the unobscured (panel (a)) or Compton-thin lightly obscured (panel (b)) sources. While there is some overlap between the CT and Compton-thin moderately obscured populations, this is predominantly due to Compton-thin moderately obscured sources with $23.5 \leqslant \log(N_H/cm^{-2}) < 24$. In light of this, appropriate selection criteria can be used to construct diagnostic regions in this parameter space that separate heavily and less obscured AGN populations. Here we define the completeness of the selection criteria as "the fraction of true heavily obscured AGNs selected," while we define purity as "the fraction of selected AGNs that are heavily obscured," i.e., the fractional contribution of heavily obscured AGNs to a diagnostic region. These definitions can be extended in an analogous fashion to the other column density bins.

Defining a horizontal cut in this parameter space,

$$\log(L_{X,Obs.}/L_{12\ \mu m}) < -1.3, \quad (5)$$

which is shown as a black dashed line in Figure 7, provides a simple yet robust method of differentiating between the most heavily and less obscured AGNs in the Swift/BAT sample. We report the sample statistics for this cut in Table 3. To derive the population statistics for Table 3 (and all percentages quoted hereafter), we calculated the median (50th percentile) value for each population in question, while the uncertainties on the fractions are the 16th and 84th quantiles of a binomial distribution, all computed following Cameron (2011). The criterion in Equation (5) yields $88.1^{+4.5}_{-5.7}$% completeness for the heavily obscured AGNs, a $60.5^{+6.3}_{-6.5}$% pure sample, and a mean column density of $\log(N_H/cm^{-2}) = 24.0 \pm 0.1$ for the diagnostic region. It is important to note that the majority of impurities selected with Equation (5) arise from AGNs with column densities $23.5 \leqslant \log(N_H/cm^{-2}) < 24.0$; the diagnostic region is in fact ~88% pure for AGNs with $\log(N_H/cm^{-2}) \geqslant 23.5$ and suffers minimal impurities from AGNs with lower column densities.

In a similar fashion, we could define a vertical cut based on the WISE colors in this space,

$$\log(L_{22\ \mu m}/L_{4.6\ \mu m}) > 0.1, \quad (6)$$

and while this criterion also yields a highly complete sample ($88^{+4.5}_{-5.7}$%) of heavily obscured AGNs, the selected sample is only $13.1^{+2.1}_{-2.0}$% pure for heavily obscured AGNs and greatly contaminated by moderately obscured, lightly obscured, and even unobscured AGNs. This is not at all surprising, given the scatter in the mid-IR ratio as demonstrated in Figures 3 and 5. Mid-IR selection alone is therefore not sufficient when attempting to select both a highly complete and fairly pure sample of heavily obscured sources.

Next, we defined a slightly more stringent box region (gray dashed–dotted and black dotted lines in Figures 7(a)–(d)), which encompasses the majority of the most heavily absorbed sources with minimal overlap with the unobscured and Compton-thin bins, using the following relations:

$$\begin{aligned} 0.1 < \log(L_{22\ \mu m}/L_{4.6\ \mu m}) < 1.0, \\ -2.8 < \log(L_{X,Obs.}/L_{12\ \mu m}) < -1.3. \end{aligned} \quad (7)$$

We report the population statistics for this diagnostic box in Table 5. This box offers a completeness of $83.0^{+5.4}_{-6.4}$% for the heavily obscured AGN population, a $62.4^{+6.5}_{-6.8}$% pure sample, and a mean column density of $\log(N_H/cm^{-2}) = 24.1 \pm 0.1$. As with Equation (5), the largest sources of impurities within this region are AGNs with $23.5 \leqslant \log(N_H/cm^{-2}) < 24$; the region is ~90% pure for AGNs with $\log(N_H/cm^{-2}) \geqslant 23.5$ and suffers few impurities from AGNs of lower column densities.

We repeated this analysis for the alternative $L_{12\ \mu m}/L_{4.6\ \mu m}$ luminosity ratio, and we show the contoured populations binned by column density along with an alternative diagnostic box for heavily absorbed sources in Figures 7(e)–(h). We construct this box with the following relations:

$$\begin{aligned} 0.0 < \log(L_{12\ \mu m}/L_{4.6\ \mu m}) < 0.75, \\ -2.8 < \log(L_{X,Obs.}/L_{12\ \mu m}) < -1.3, \end{aligned} \quad (8)$$

and we find that this box yields a completeness of $80.5^{+5.7}_{-6.7}$% for heavily absorbed AGNs, a purity of $59.4^{+6.5}_{-6.8}$%, and a median column density of $\log(N_H/cm^{-2}) = 24.0 \pm 0.1$. Again, AGNs with column densities $23.5 \leqslant \log(N_H/cm^{-2}) < 24$ contribute the most to the impurity of the sample, while AGNs with lower column densities do not contribute as significantly.

The diagnostic metrics defined above—developed using the well-constrained X-ray and mid-IR properties previously found for Swift/BAT AGNs (e.g., Ricci et al. 2017a; Ichikawa et al. 2017)—carve out parameter spaces that yield fairly complete and pure samples of heavily obscured AGNs, offering an efficient and effective method for identifying heavily obscured or CT AGN candidates, particularly in large samples of AGNs.

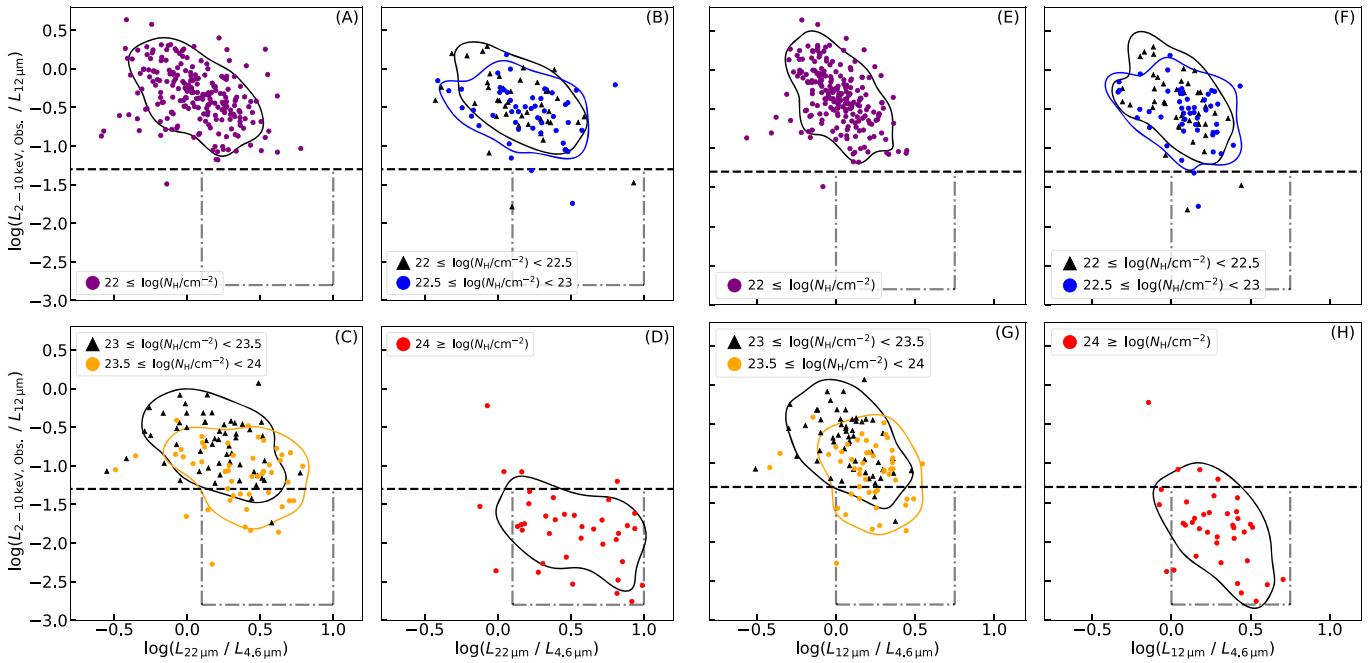

Figure 7. The $L_{22\ \mu m}/L_{4.6\ \mu m}$ (panels (a)–(d)) and $L_{12\ \mu m}/L_{4.6\ \mu m}$ (panels (e)–(h)) diagnostics for AGNs in the Swift/BAT sample binned by N_H, where we have unobscured (panels (a) and (e); $\log(N_H/cm^{-2}) < 22$), Compton-thin lightly obscured (panels (b) and (f); $22 \leqslant \log(N_H/cm^{-2}) < 23$), Compton-thin moderately obscured (panels (c) and (g); $23 \leqslant \log(N_H/cm^{-2}) < 24$), and heavily obscured to CT (panels (d) and (h); $\log(N_H/cm^{-2}) \geqslant 24$). The Compton-thin bins are broken into two sub-bins each: $22 \leqslant \log(N_H/cm^{-2}) < 22.5$ (black points in panels (b) and (f)), $22.5 \leqslant \log(N_H/cm^{-2}) < 23$ (blue points), $23 \leqslant \log(N_H/cm^{-2}) < 23.5$ (black points in panels (c) and (g)), and $23.5 \leqslant \log(N_H/cm^{-2}) < 24$ (orange points). Contours were computed to encompass ∼68% of the population for each respective bin or sub-bin. Note that, in general, the most obscured sources tend to populate a different region of the parameter space than the unobscured and Compton-thin lightly obscured sources, while there is some overlap with Compton-thin moderately obscured sources.

Table 3
$\log(L_{X,Obs.}/L_{12\ \mu m}) \leqslant -1.3$ Diagnostic Cut

$\log(N_H/cm^{-2})$ (1)	Completeness (2)	Purity (3)
⩾24.0	$88.1^{+4.5}_{-5.7}$	$60.5^{+6.3}_{-6.5}$
<24.0	$5.4^{+1.2}_{-1.0}$	$39.5^{+6.5}_{-6.3}$
[23.0, 24.0)	$16.3^{+3.7}_{-3.3}$	$30.8^{+6.2}_{-5.8}$
[23.5, 24.0)	$30.5^{+6.6}_{-6.1}$	$27.3^{+6.1}_{-5.6}$
[23.0, 23.5)	$4.6^{+3.2}_{-2.2}$	$4.7^{+3.3}_{-2.2}$
[22.0, 23.0)	$5.0^{+2.6}_{-1.9}$	$8.1^{+4.0}_{-3.1}$
[22.5, 23.0)	$5.3^{+3.7}_{-2.5}$	$4.7^{+3.3}_{-2.2}$
[22.0, 22.5)	$6.0^{+4.2}_{-2.9}$	$4.7^{+3.3}_{-2.2}$
<22.0	$0.8^{+0.7}_{-0.4}$	$2.9^{+2.7}_{-1.7}$

Note. Statistics derived from the $\log(L_X^{Obs.}/L_{12\mu m}) < -1.3$ threshold, defined in Section 3 (Equation (5)), for various N_H bins and sub-bins. Column 1: N_H bin. Column 2: completeness, or the fraction of AGNs selected (per column density bin). Column 3: purity of the sample, or the percentage contribution to the diagnostic box.

Table 4
$\log(L_{22\ \mu m}/L_{4.6\ \mu m}) \geqslant 0.1$ Diagnostic Cut

$\log(N_H/cm^{-2})$ (1)	Completeness (2)	Purity (3)
⩾24.0	$88.1^{+4.5}_{-5.7}$	$13.1^{+2.1}_{-2.0}$
<24.0	$55.0^{+2.4}_{-2.4}$	$86.9^{+2.0}_{-2.1}$
[23.0, 24.0)	$75.4^{+3.9}_{-4.3}$	$30.8^{+2.9}_{-2.8}$
[23.5, 24.0)	$81.2^{+5.0}_{-5.8}$	$15.7^{+2.3}_{-2.1}$
[23.0, 23.5)	$69.7^{+5.7}_{-6.2}$	$15.3^{+2.3}_{-2.1}$
[22.0, 23.0)	$56.4^{+5.0}_{-5.1}$	$19.8^{+2.5}_{-2.4}$
[22.5, 23.0)	$60.9^{+6.7}_{-6.9}$	$11.6^{+2.0}_{-1.9}$
[22.0, 22.5)	$51.1^{+7.4}_{-7.4}$	$8.5^{+1.8}_{-1.6}$
<22.0	$44.3^{+3.3}_{-3.3}$	$36.8^{+3.0}_{-2.9}$

Note. Statistics derived from the mid-IR $\log(L_{22\ \mu m}/L_{4.6\ \mu m}) \geqslant 0.1$ criteria (without invoking any cut in $\log[L_X^{Obs.}/L_{12\mu m}]$) defined in Section 3 (Equation (6)) for various N_H bins and sub-bins. Columns 1–3: same as in Table 3.

4. Discussion

4.1. The Physical Origin of the Trend in WISE Ratios as a Function of N_H

The observed trend of the 22 μm/4.6 μm and 12 μm/4.6 μm WISE ratios increasing with column density can be readily understood from dust absorption and emission properties and basics of the radiation transfer. For media optically thin to the mid-IR radiation, the shape of the resulting spectral energy distribution (SED) will be determined predominantly by the dust temperature and its gradient throughout the dusty structure. If the dusty medium is optically thick to its own radiation, the outgoing emission will be reshaped for a number of reasons. (i) Warm dust emission at shorter wavelengths will be absorbed and reemitted at longer wavelengths. (ii) Dust emission at shorter wavelengths will suffer more extinction than the long-wavelength emission, owing to the wavelength-dependent extinction for typical AGN dust (Laor & Draine 1993). (iii) Warm dust emission originates closer to the inner rim of the torus, while colder emission originates farther out. As a consequence, longer-wavelength

Table 5
$L_{22\ \mu m}/L_{4.6\ \mu m}$ Diagnostic Box Statistics

$\log(N_H/cm^{-2})$ (1)	Completeness (2)	Purity (3)
$\geqslant$24.0	$83.0^{+5.4}_{-6.4}$	$62.4^{+6.5}_{-6.8}$
<24.0	$4.7^{+1.1}_{-1.0}$	$37.6^{+6.8}_{-6.5}$
[23.0, 24.0)	$15.4^{+3.6}_{-3.2}$	$31.8^{+6.6}_{-6.1}$
[23.5, 24.0)	$28.6^{+6.5}_{-6.0}$	$28.0^{+6.4}_{-5.9}$
[23.0, 23.5)	$4.6^{+3.2}_{-2.2}$	$5.1^{+3.6}_{-2.5}$
[22.0, 23.0)	$3.9^{+2.3}_{-1.7}$	$7.0^{+4.0}_{-3.0}$
[22.5, 23.0)	$5.3^{+3.7}_{-2.5}$	$5.1^{+3.6}_{-2.5}$
[22.0, 22.5)	$3.8^{+3.5}_{-2.2}$	$3.2^{+3.0}_{-1.8}$
<22.0	$0.3^{+0.5}_{-0.2}$	$1.3^{+2.1}_{-1.0}$

Note. Statistics derived from the diagnostic box developed for the $L_{22\ \mu m}/L_{4.6\ \mu m}$ luminosity ratio (defined by Equation (7) in Section 3) for various N_H bins and sub-bins. Columns 1–3: same as in Table 3.

mid-IR radiation has to travel a shorter path through the dust before reaching us and thus suffers even less extinction than the emission of shorter wavelengths. These three effects result in an increased ratio of longer-to-shorter-wavelength mid-IR emission and scale with the column density of the medium through which the X-ray radiation is traversing. (iv) Additionally, a disklike molecular structure in hydrostatic equilibrium is expected to have a vertical gradient (Hönig 2019). In this case, the observed trend of increasing WISE ratios with increasing N_H can be explained simply as an inclination effect: the closer our viewing angle is to the equator, the higher the column density is along the line of sight, and, at the same time, the dust emission becomes "redder." All of these effects contribute to the observed trend of increasing WISE ratios with N_H and also explain why the effect is more pronounced in the 22 μm/4.6 μm ratio than in the 12 μm/4.6 μm luminosity ratio (for illustration, see torus model SEDs in, e.g., Hönig & Kishimoto 2010; Stalevski et al. 2012).

There are a few caveats. The dust emission is often degenerate, as SEDs of similar shape can be produced by different combinations of the geometrical and physical parameters of the torus, some of which can conspire to work against or hide the trend in luminosity ratios. However, the above reasoning should hold in general, since it relies on universal radiative transfer effects. Another deviation can be introduced by the presence of silicate dust grains, which exhibit a strong increase of absorption efficiency around 10 and 18 μm. The apparent strength of these features appearing in an SED depends on several factors, including the amount of silicates, grain size distribution, and radiative transfer effects.

We illustrate these effects in Figure 6 with a black dashed line, which represents a theoretical expectation for a very simple model: monochromatic radiation passing through a homogeneous screen of dust. For this example, we assumed a typical Galactic interstellar dust mixture of silicates and graphite (e.g., Stalevski et al. 2016). The grain size distributions are from Mathis et al. (1977), and the optical properties are from Laor & Draine (1993) and Li & Draine (2001). The conversion between the optical depth and N_H assumes a Galactic relation between extinction and column density found by Predehl & Schmitt (1995). We see that the theoretical curve is following the trend of the data at lower column densities but reaching the breaking point sooner. This is because the simple dust screen model does not account for a number of radiative transfer effects (self-consistent absorption and reemission of the thermal IR radiation), which, together with the geometry of the dusty medium and orientation, shape the resulting SED and thus the observed trend of luminosity ratios with column density.

4.2. Comparison to Asmus et al. (2015)

Using subarcsecond-resolution mid-IR observations—which enabled the isolation of the nuclear mid-IR emission ($F^{nuc}_{12\ \mu m}$)—Asmus et al. (2015) found a significant correlation between $\log(F^{nuc}_{12\ \mu m}/F^{obs}_{2-10\ keV})$ and $\log(N_H/cm^{-2})$ for 53 AGNs with reliable X-ray observations and column densities $\log(N_H/cm^{-2}) > 22.8$, which was expressed as (see Equation (6) in Asmus et al. 2015)

$$\log\left(\frac{N_H}{22.8\ cm^{-2}}\right) = (0.14 \pm 0.11) + (0.67 \pm 0.12)\log\left(\frac{F^{nuc}_{12\ \mu m}}{F^{obs}_{2-10\ keV}}\right). \quad (9)$$

This expression is plotted in Figure 5 (dashed red line) along with our Equation (2) (solid orange line) and the Swift/BAT sample. Along with values of $\log(N_H/cm^{-2})$ derived using Equation (2) in Section 3.1, we use the relation from Asmus et al. (2015) to derive values of $\log(N_H/cm^{-2})$ and the uncertainties for specific values of $\log(L_{X,Obs.}/L_{12\ \mu m})$ in order to compare to our own results. Despite the fact that Asmus et al. (2015) removed AGNs with $\log(N_H/cm^{-2}) < 22.8$ and utilized subarcsecond-resolution mid-IR emission (whereas in this work, we utilized lower angular resolution mid-IR photometry for the Swift/BAT sample), it does appear that the two relations generally agree (within the uncertainties) for ratios of $-0.75 \lesssim \log(L_{X,Obs.}/L_{12\ \mu m}) \lesssim -3.0$. The two relations differ more severely for higher ratios of $\log(L_{X,Obs.}/L_{12\ \mu m})$, though this is expected due to (1) the wide range of ratios that unobscured AGNs exhibit and (2) the fact that our relation turns over to account for less obscured sources, while the Asmus et al. (2015) relation does not take into account less obscured sources.

4.3. Diagnosing Column Densities with Uncertain Dust Heating Sources

While the diagnostic boxes defined in Section 3 provide a reliable way to identify the most heavily obscured AGNs, star formation activity can contribute nonnegligibly to the mid-IR colors of an AGN host. The mid-IR colors assumed to originate from the AGN itself could therefore be overestimated without performing detailed SED fitting to differentiate between the AGN and star formation contributions to the mid-IR continuum. Furthermore, Satyapal et al. (2018) demonstrated, using *Cloudy* (Ferland et al. 2013, 2017) radiative transfer models, that heavily obscured star formation activity can actually mimic the mid-IR colors of AGNs. These two points suggest that our diagnostic boxes defined in Section 3 may (1) misdiagnose the column density of an AGN if significant star formation is present, as the contaminating stellar emission could lead to much redder colors than the AGN intrinsically exhibits, or (2) mislead us to think an AGN is present in cases where the dominant dust heating sources are actually stellar-related rather than AGN-related (Satyapal et al. 2018). To

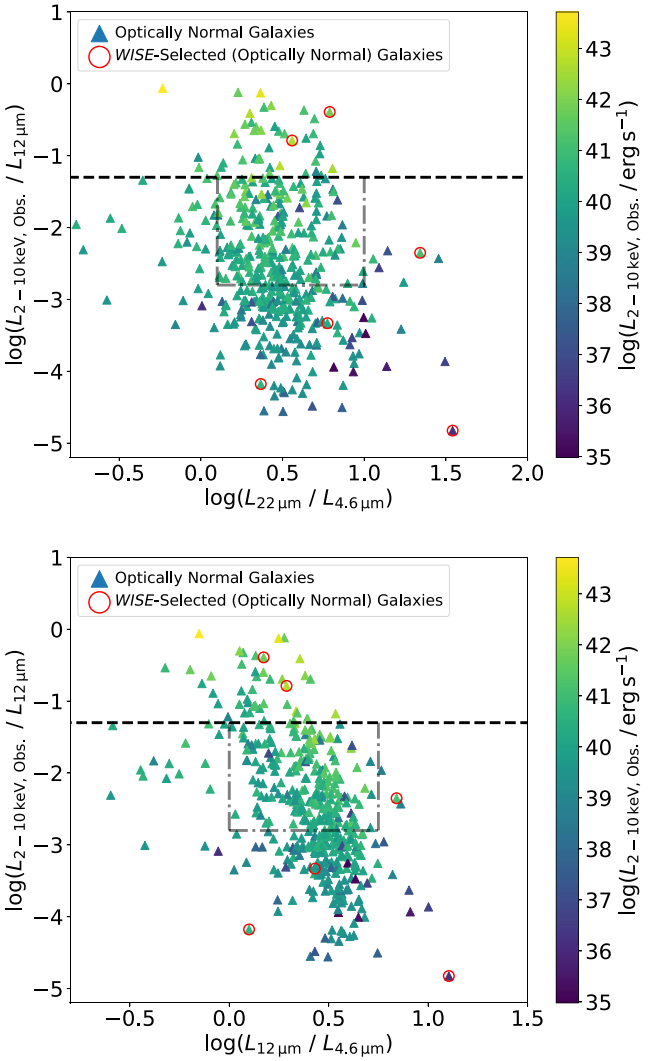

Figure 8. The top (bottom) panel shows a diagnostic box defined in Figure 7 and Equation (7) (Equation (8)) for the $L_{22\,\mu m}/L_{4.6\,\mu m}$ ($L_{12\,\mu m}/L_{4.6\,\mu m}$) ratio with a population of star-forming galaxies (see Section 4.3) overlaid as triangles. The horizontal dashed black line is given by Equation (5). The observed X-ray luminosity is denoted on the auxiliary axis. The diagnostics presented here cannot unambiguously differentiate between AGNs and star-forming systems, since a significant fraction of the star-forming galaxy population falls within the absorption diagnostic box. This contamination can be mitigated with a mid-IR WISE cut of W1 − W2 > 0.8 (Stern et al. 2012); only six optically normal galaxies satisfy this mid-IR criterion (red open circles), and these systems fall outside of the diagnostic box defined by Equation (7) (Equation (8)).

investigate this potential contamination of the diagnostic boxes, we constructed a catalog of optically selected galaxies whose optical spectroscopic line ratios suggest that star formation dominates the observed emission, and we examined methods—for example, mid-IR or X-ray selection criteria—through which this contamination could be mitigated.

Beginning with the MPA-JHU catalog of galaxy properties (from the Sloan Digital Sky Survey (SDSS) Data Release 8; Aihara et al. 2011), we first selected systems with redshifts $z < 0.1$ and included only systems that are classified as star-forming systems ("BPTClass" = 1) based upon their Baldwin–Phillips–Terlevich (BPT; Baldwin et al. 1981) optical spectroscopic emission line ratios. We also removed any systems with QSO and AGN flags within the "TARGETTYPE," "SPECTROTYPE," and "SUBCLASS" columns and then narrowed the sample to only systems with WISE and X-ray counterparts, the latter of which are drawn from the 4XMM point-source catalog (Webb et al. 2020). These criteria yielded a full parent sample of 448 galaxies that we assume are "purely" star-forming systems based upon optical spectroscopic measurements. We make no distinction between morphological classes of galaxies.

We plot our population of optically selected star-forming galaxies (color coded according to the observed X-ray luminosity) along with the $L_{22\,\mu m}/L_{4.6\,\mu m}$ and $L_{12\,\mu m}/L_{4.6\,\mu m}$ diagnostic boxes in Figure 8. While star formation–dominated galaxies tend to exhibit lower ratios of $\log(L_{X,Obs.}/L_{12\,\mu m})$ than the majority of the Swift/BAT sample, they do tend to exhibit similar X-ray deficits, as well as $L_{22\,\mu m}/L_{4.6\,\mu m}$ and $L_{12\,\mu m}/L_{4.6\,\mu m}$ mid-IR colors, as those exhibited by the heavily obscured Swift/BAT AGNs; in fact, $44.4\% \pm 2.3\%$ of this star-forming population overlaps the $L_{22\,\mu m}/L_{4.6\,\mu m}$ diagnostic region, while $47.1^{+2.3}_{-2.3}$ % of the population overlaps the $L_{12\,\mu m}/L_{4.6\,\mu m}$ region. We therefore caution that this diagnostic is emphatically not designed to differentiate between star-forming and AGN-dominated systems and should not be used as a diagnosis of the dominant dust heating source. Nevertheless, the contamination from optically selected star-forming systems can be mitigated through the use of reliable mid-IR and X-ray selection criteria traditionally used for identifying AGNs.

We applied the two-band WISE AGN selection cut (W1 [3.4 μm] – W2 [4.6 μm] > 0.8) from Stern et al. (2012) to the sample of star-forming galaxies, which removed all but six systems (red open circles in Figure 8). As expected, requiring a traditional mid-IR AGN selection criterion eliminates virtually all contamination by optically selected star-forming systems within the diagnostic boxes. While six star-forming galaxies ($1.5^{+0.6}_{-0.5}\%$ of the total population) succeed in meeting the Stern et al. (2012) cut, these do still fall outside of our diagnostic boxes.[26] Thus, use of mid-IR AGN selection tools could be used to avoid misdiagnosing the dominant photoionization process of the sources within the diagnostic regions. However, it is important to bear in mind that the relation between $L_{X,Obs.}/L_{12\,\mu m}$, $L_{22\,\mu m}/L_{4.6\,\mu m}$ (and $L_{12\,\mu m}/L_{4.6\,\mu m}$), and N_H holds true for both WISE- and non-WISE-selected AGNs (see the Appendix); therefore, requiring a WISE cut could generally remove true AGNs, as well as star-forming systems. For example, imposing the W1 – W2 > 0.8 cut on the Swift/BAT sample examined in this work would remove 240 systems (or $52.6^{+2.3}_{-2.3}\%$ of the parent sample of 456 AGNs); in the parent sample of 456, there are 71 AGNs that possess column densities in excess of 5×10^{23} cm^{-2}, and 40 of these would be removed with this mid-IR cut.

We also found that requiring an observed X-ray luminosity of $L_{X,Obs.} > 10^{42}$ erg s^{-1} removes nearly all of the optically star-forming population from the diagnostic region (five galaxies, or $1.3^{+0.6}_{-0.5}\%$, remain within the $L_{22\,\mu m}/L_{4.6\,\mu m}$ diagnostic box), though this method must also be used judiciously to avoid removing heavily obscured AGNs, which could exhibit lower X-ray luminosities.

Ideally, use of this diagnostic should be limited to systems whose dominant photoionization processes are unambiguous or

[26] Four out of six sources do fall below our cut in $L_{X,Obs.}/L_{12\,\mu m}$: (1) a compact star-forming region in a galaxy ∼318 Mpc away, (2) a galaxy at $z = 0.07$, (3) a pair of merging galaxies at $z = 0.058$, and (4) a pair of merging galaxies that actually host a candidate dual AGN at $z = 0.055$ (Pfeifle et al. 2019).

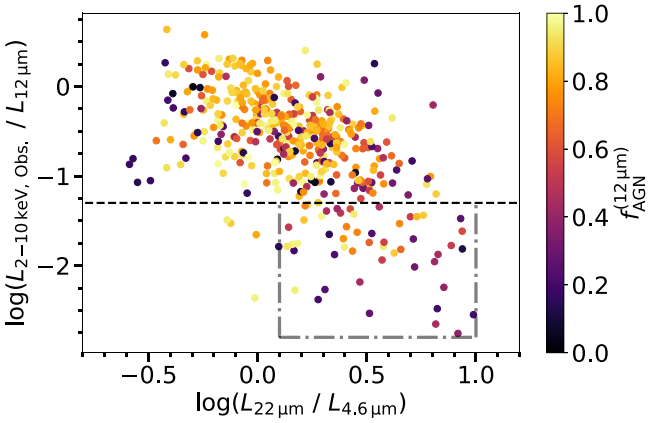

Figure 9. Logarithmic $L_{\mathrm{X,Obs.}}/L_{12\ \mu\mathrm{m}}$ vs. $L_{22\ \mu\mathrm{m}}/L_{4.6\ \mu\mathrm{m}}$ ratios of the Swift/BAT AGN sample, where the data are color coded according to the fractional contribution of the AGN 12 μm emission to the total observed 12 μm emission ($f_{\mathrm{AGN}}^{12\ \mu\mathrm{m}}$). While there is no clear offset in this parameter space between AGN- and host-dominated systems, several of the most heavily obscured AGNs (i.e., sources with significant X-ray deficits and $\log(L_{22\ \mu\mathrm{m}}/L_{4.6\ \mu\mathrm{m}}) > 0.1$) do reside in systems where the host dominates the 12 μm emission.

for which detailed SED fitting can be performed to differentiate between AGN and host emission. Otherwise, we recommend proceeding cautiously, taking into account the various caveats outlined above to avoid inaccurate estimations of the obscuration along the line of sight.

4.4. Mid-IR Emission Contributions from Galaxies Hosting Obscured AGNs

The realization in Section 4.3 that optically star-forming galaxies, which presumably do not host AGNs, can exhibit luminosity ratios similar to those exhibited by more heavily obscured or CT Swift/BAT AGNs raises the intriguing point of how much host galaxies may contribute to the observed luminosity ratios derived for the Swift/BAT AGNs. Figure 9 shows the $\log(L_{\mathrm{X,Obs.}}/L_{12\ \mu\mathrm{m}})$ and $\log(L_{22\ \mu\mathrm{m}}/L_{4.6\ \mu\mathrm{m}})$ ratios of the Swift/BAT AGNs and is color coded according to the fractional contribution by the AGN to the observed 12 μm emission ($f_{\mathrm{AGN}}^{12\ \mu\mathrm{m}}$) derived through detailed SED fitting in Ichikawa et al. (2019). While host-dominated systems at 12 μm ($f_{\mathrm{AGN}}^{12\ \mu\mathrm{m}} < 0.5$) can be found across this parameter space, a significant fraction ($43.3^{+6.9}_{-6.7}$%, 22 out of 51) of AGNs within the diagnostic region (Equation (7)) reside in host-dominated systems. This suggests that the host galaxies could contribute significantly to the observed mid-IR colors of the heavily obscured AGN population in particular, presumably via dust emission heated through star formation.

Ichikawa et al. (2019) provided decomposed logarithmic AGN 12 μm luminosities for the Swift/BAT AGNs, which we can use here to examine how the $\log(L_{\mathrm{X,Obs.}}/L_{12\ \mu\mathrm{m}})$ ratios may change if we use the AGN 12 μm luminosity ($L_{12\ \mu\mathrm{m,AGN}}$) instead of the total observed 12 μm luminosity ($L_{12\ \mu\mathrm{m}}$). Figure 10 (top panel) shows that host-dominated systems are predominantly occupied by AGNs with $\log(N_{\mathrm{H}}/\mathrm{cm}^{-2}) \gtrsim 22.5$; half of the CT Swift/BAT AGNs reside in host-dominated systems. After recalculating the luminosity ratio using $L_{12\ \mu\mathrm{m,AGN}}$ instead (bottom panel), host-dominated systems exhibit a shift toward higher luminosity ratios, with an average difference in ratio of $\Delta\log(L_{\mathrm{X,Obs.}}/L_{12\ \mu\mathrm{m}}) \approx 0.5$ for AGNs with $f_{\mathrm{AGN}}^{12\ \mu\mathrm{m}} < 0.5$, although we note that these shifts are not limited only to heavily obscured AGNs. Here we have

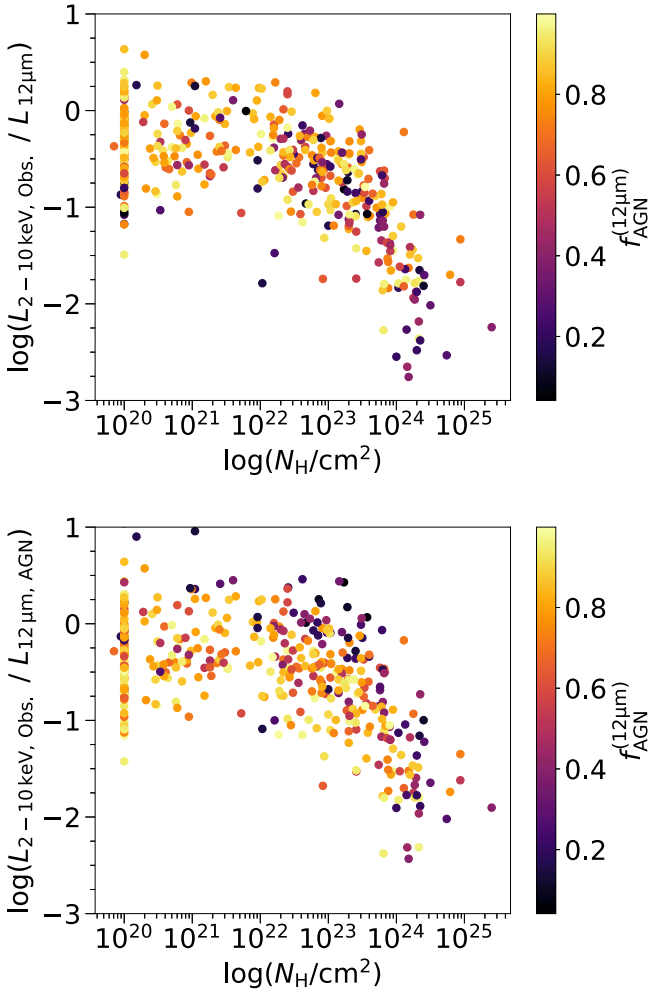

Figure 10. The $\log(N_{\mathrm{H}}/\mathrm{cm}^{-2})$ vs. $\log(L_{\mathrm{X,Obs.}}/L_{12\ \mu\mathrm{m}})$ for (top) the total 12 μm emission and (bottom) the decomposed AGN 12 μm emission from Ichikawa et al. (2019). The auxiliary axes represent the fractional contribution by the AGN to the total observed 12 μm emission. (Top) As is already known, $\log(L_{\mathrm{X,Obs.}}/L_{12\ \mu\mathrm{m}})$ decreases with increasing column density; however, a significant number of obscured and CT AGNs contribute less than 50% of the total observed 12 μm ($f_{\mathrm{AGN}}^{12\ \mu\mathrm{m}}$). (Bottom) The relationship between $\log(L_{\mathrm{X,Obs.}}/L_{12\ \mu\mathrm{m}})$ and $\log(N_{\mathrm{H}}/\mathrm{cm}^{-2})$ is still present when recalculating the ratio using the decomposed AGN 12 μm luminosity ($L_{12\ \mu\mathrm{m,AGN}}$), although obscured and CT AGNs exhibit smaller deficits than when using the total 12 μm luminosity. Host galaxies can therefore contribute significantly to the observed X-ray–to–mid-IR ratios of AGNs, especially CT AGNs.

assumed that the X-ray emission is AGN-dominated, rather than host-dominated; in reality, if some portion of the X-ray emission is due to the host as well, the observed ratio shifts will not be as large.

Figure 9 demonstrates that host galaxies do indeed contribute significantly to the diagnostic ratios probed in this work, at least for systems in which the host dominates the mid-IR emission at 12 μm. In these cases, the host contribution to the mid-IR leads to a perceived larger X-ray deficit for the AGN at a given column density. It does appear, though, that generally, this effect actually works in our favor when attempting to identify CT AGNs, as these more severe X-ray deficits and presumably "redder" mid-IR colors aid in separating this population from less obscured populations in color space. Decomposed AGN 22 and 4.6 μm luminosities were not included in Table 1 of Ichikawa et al. (2019) and therefore could not be examined in a similar fashion here. While it is

Table 6
$L_{12\ \mu m}/L_{4.6\ \mu m}$ Diagnostic Box Statistics

$\log(N_H/cm^{-2})$ (1)	Completeness (2)	Purity (3)
$\geqslant$24.0	$80.5^{+5.7}_{-6.7}$	$59.4^{+6.5}_{-6.8}$
<24.0	$5.2^{+1.1}_{-1.0}$	$40.6^{+6.8}_{-6.5}$
[23.0, 24.0)	$16.3^{+3.7}_{-3.3}$	$33.1^{+6.6}_{-6.2}$
[23.5, 24.0)	$30.5^{+6.6}_{-6.1}$	$29.4^{+6.4}_{-5.9}$
[23.0, 23.5)	$4.6^{+3.2}_{-2.2}$	$5.0^{+3.5}_{-2.4}$
[22.0, 23.0)	$5.0^{+2.6}_{-1.9}$	$8.8^{+4.3}_{-3.3}$
[22.5, 23.0)	$5.3^{+3.7}_{-2.5}$	$5.0^{+3.5}_{-2.4}$
[22.0, 22.5)	$6.0^{+4.2}_{-2.9}$	$5.0^{+3.5}_{-2.4}$
<22.0	$0.3^{+0.5}_{-0.2}$	$1.3^{+2.1}_{-1.0}$

Note. Breakdown of the statistics derived from the diagnostic box developed for the $L_{12\ \mu m}/L_{4.6\ \mu m}$ luminosity ratio (defined by Equation (8) in Section 3) for various N_H bins and sub-bins. Columns 1–3: same as in Table 3.

beyond the scope of this paper, an analysis of the interplay between the mid-IR colors, host galaxy emission, and AGN emission with regard to the selection diagnostics presented in this work should be performed more rigorously in a future study.

4.5. Comparison to Kilerci Eser et al. (2020)

In a very recent study, Kilerci Eser et al. (2020) selected a subsample of the 105 month Swift/BAT catalog (Oh et al. 2018) and proposed a new selection method for CT AGNs using mid- and far-IR photometry. They reported, as we do in Section 3 of this study, a shift in IR colors (specifically mid- and far-IR) toward "redder" colors with increasing column density, and they defined a physically motivated color–color diagram (see Figure 11, hereafter F11, in Kilerci Eser et al. 2020) and selection method using the [9 μm]–[22 μm] and [22 μm]–[90 μm] colors. Of the 32 CT Swift/BAT AGNs for which there exists the relevant photometry, these selection criteria identify four CT AGNs (a success rate of $14.0^{+6.6}_{-5.2}$%). However, it is evident from F11 that these color cuts cannot reliably distinguish between unobscured, obscured, and CT AGNs, as the AGNs from these three different obscuration bins largely occupy the same [9 μm]–[22 μm] and [22 μm]–[90 μm] parameter space. In the case of Swift/BAT, the color–color criteria proposed by Kilerci Eser et al. (2020) yield a far lower success rate of identifying heavily obscured and CT AGNs than the criteria set forth in this work (e.g., Equations (7) and (8); see Tables 3, 5, and 6).

To further test their diagnostic, they applied these color selection criteria to the AKARI IR galaxy catalog developed in Kilerci Eser & Goto (2018), which contains over 17,000 galaxies, and recovered one known CT AGN (NGC 4418; e.g., Sakamoto et al. 2013).[27] The remainder of the IR galaxy sample of Kilerci Eser & Goto (2018) is represented with blue contours in F11 that partially overlap a significant number of Swift/BAT CT, obscured, and unobscured AGNs, suggesting that some portion of these IR galaxies may in fact host heavily obscured AGNs. Despite finding a few cases of CT AGNs

[27] The selection criteria also recover two other sources: NGC 7714, an unobscured AGN (Gonzalez-Delgado et al. 1995; Smith et al. 2005), and NGC 1614, which has no clear evidence of an AGN (e.g., Xu et al. 2015; Pereira-Santaella et al. 2011; Herrero-Illana et al. 2014).

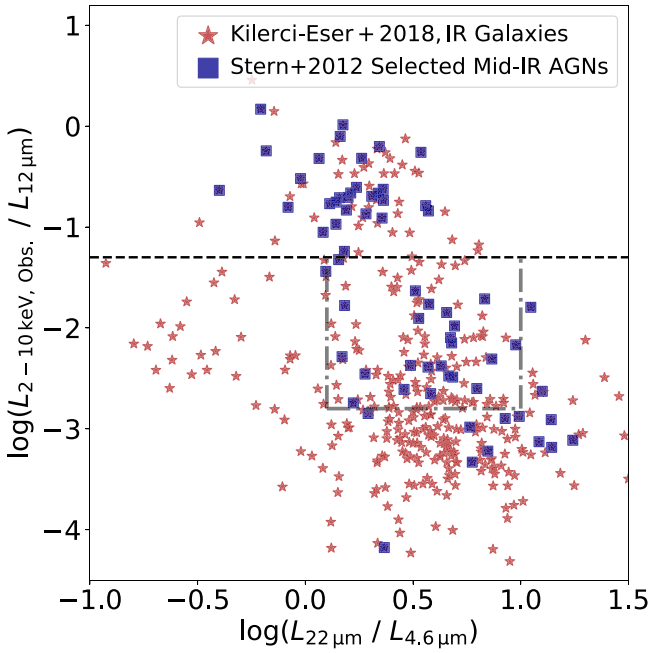

Figure 11. The $L_{X,Obs.}/L_{12\ \mu m}$ vs. $L_{22\ \mu m}/L_{4.6\ \mu m}$ ratios for the IR galaxies (red stars) cataloged by Kilerci Eser & Goto (2018), along with the obscuration diagnostics established in Equations (5) and (7). After applying the Stern et al. (2012) mid-IR cut to search for AGNs within the sample, we find a significant population of candidate heavily obscured or CT AGNs contained within the Kilerci Eser & Goto (2018) catalog, a result not found using the mid-to-far-IR color–color criteria proposed by Kilerci Eser et al. (2020). See Table 7 for more details on these AGNs.

between the Swift/BAT and Kilerci Eser & Goto (2018) samples, the diagnostic criteria set forth in Kilerci Eser et al. (2020) do not appear to provide a complete or reliable (see Section 5.4 of Kilerci Eser et al. 2020) method of selecting CT AGNs.

As an additional comparison between our selection method and that proposed by Kilerci Eser et al. (2020), we turned our attention to the IR galaxy catalog from Kilerci Eser & Goto (2018). We matched this sample to the AllWISE catalog and the 4XMM DR9 XMM-Newton Serendipitous Source Catalog (Webb et al., submitted) using a match radius of 10″ for each, which yielded a sample of 401 local ($z < 0.1$) IR galaxies with XMM-Newton and WISE detections. In Figure 11, we show the resulting sample of IR galaxies (red stars), along with our diagnostic criteria from Equations (5) and (7). As in Section 4.3, it is impossible to discern whether or not any of these galaxies host AGNs without a reliable method for removing star formation–dominated systems. We tried four different mid-IR AGN selection criteria, defined in Jarrett et al. (2011), Stern et al. (2012), Assef et al. (2018), and Satyapal et al. (2018; with the understanding that some heavily obscured AGNs will be missed with this simple approach), and in all four cases, we recover a significant number of candidate heavily obscured or CT AGNs. We show the mid-IR AGNs selected as a result of the Stern et al. (2012) cut in Figure 11 (blue squares); these candidate CT AGNs likely inhabited the blue contoured prominence that overlapped the Swift/BAT AGNs in F11 but were missed due to fact that they did not satisfy the criteria proposed by Kilerci Eser et al. (2020).

Table 7 lists the 36 candidate CT AGNs selected from Kilerci Eser & Goto (2018) using the $L_{22\ \mu m}/L_{4.6\ \mu m}$ diagnostic region and at least one of the mid-IR selection cuts listed

above. We include in the table the source coordinates, redshifts, luminosity ratios, and alternative identifiers, and we also categorize the column densities of the sources (using the column density bins defined in Section 3.3) based upon any available measurements in the literature. Of the candidates that have inferred or directly measured column densities in the literature (24/36), we find eight CT, six moderately obscured, two lightly obscured, and three unobscured AGNs, while the remaining five AGNs have conflicting measurements of $N_{\rm H}$ in the literature (all five of which have been reported as CT at least once in the past).[28] Therefore, we conclude that our diagnostic criteria proposed in Equations (5), (7), and (8) offer a more reliable method for identifying candidate CT AGNs than the mid-to-far-IR color criteria proposed by Kilerci Eser et al. (2020).

In light of Section 4.4, we caution that some portion of these AGNs may not dominate the observed 12 μm emission and therefore may exhibit larger X-ray deficits and redder mid-IR colors than might be expected for the AGN alone due to additional mid-IR contributions from the host galaxy.

4.6. Diagnosis of N_H in the XMM XXL Field

To test the power of our absorption diagnostic, we turn our attention to its application in the XMM XXL-N field (Pierre et al. 2016, 2017). Menzel et al. (2016) presented a rigorous multiwavelength analysis of 8445 X-ray sources detected by XMM-Newton in an 18 deg^2 area of the XMM XXL-N field with a limiting flux of $F_{0.5-10\,\rm keV} > 10^{-15}$ erg cm^{-2} s^{-1}, providing optical SDSS and mid-IR WISE counterparts to the XMM-Newton sources. In a complementary investigation, Liu et al. (2016) presented a thorough X-ray spectral analysis of the 2512 XXL-N AGNs, deriving the spectral properties (e.g., photon index Γ, $N_{\rm H}$, $L_{\rm X,Obs.}$) for those AGNs using a Bayesian statistical approach contained within the Bayesian X-ray Astronomy software package (Buchner et al. 2014).

We combined the catalogs from Menzel et al. (2016) and Liu et al. (2016) to obtain the observed 2–10 keV luminosities and mid-IR WISE magnitudes, from which we derived the relevant luminosity ratios examined in Section 3. Initially, we limited the XXL-N sample to only local ($z < 0.1$) AGNs, and, as with the Swift/BAT AGNs, we did not employ any mid-IR or X-ray selection criteria. We plot the resulting luminosity ratios of the low-redshift AGNs from the XXL-N field in the left panel of Figure 12, along with our $L_{22\,\mu\rm m}/L_{4.6\,\mu\rm m}$ diagnostic box (Equation (7)) and horizontal cut in $L_{\rm X,Obs.}/L_{12\,\mu\rm m}$ (Equation (5)). The data and auxiliary axis in Figure 12 are color coded to represent the derived 50th percentile $N_{\rm H}$ values from the Liu et al. (2016) catalog, and the markers denote the obscuration bin for each AGN. In the right panel of Figure 12, we plot the $L_{\rm X,Obs.}/L_{12\,\mu\rm m}$ ratio against the derived $\log(N_{\rm H}/{\rm cm}^{-2})$ values from Liu et al. (2016), where the error bars represent the 16th and 84th percentiles and the data points use the same marker and color scheme as the left panel. A dearth of low-redshift AGNs in the XXL-N field is immediately apparent, and while it appears that most of the more obscured AGNs do exhibit "redder" colors, there is some overlap in $L_{\rm X,Obs.}/L_{12\,\mu\rm m}$ ratios exhibited by AGNs of starkly different obscuration bins, e.g., heavily obscured and unobscured AGNs. Unfortunately, we cannot draw definitive conclusions about the reliability of our diagnostic for the XXL-N field with such poor AGN statistics.

We repeated this analysis for the entire sample of XXL-N AGNs, breaking the sample into redshift bins of $\Delta z = 0.5$ each. While a small number of obscured AGNs overlap with the diagnostic region defined by Equation (7), the majority of the heavily absorbed AGNs still occupy the same parameter space as the Compton-thin and unobscured AGNs, even in the local ($z < 0.5$) redshift bin, in stark contrast to the results found with the Swift/BAT AGNs. We find a very similar result when examining the $L_{12\,\mu\rm m}/L_{4.6\,\mu\rm m}$ diagnostic ratio. Due to the fact that at higher redshift, the $L_{22\,\mu\rm m}/L_{4.6\,\mu\rm m}$ and $L_{12\,\mu\rm m}/L_{4.6\,\mu\rm m}$ diagnostics do not correspond to the same wavelength ranges as they do at local redshifts, we then turned to the luminosity ratio of $L_{12\,\mu\rm m}/L_{3.4\,\mu\rm m}$. Yet again, the heavily absorbed AGNs generally occupy the same parameter space as unobscured AGNs. The spectral curvature method (Koss et al. 2016) may provide a more effective means of selecting heavily obscured AGNs at higher redshift in the XXL-N field, and indeed, Baronchelli et al. (2017) demonstrated its effectiveness in selecting high-redshift ($z > 2$) CT AGNs in both the Chandra Deep Field South and the Chandra COSMOS legacy survey.

There are a few explanations for why the luminosity ratios of the XXL-N AGNs do not as clearly differentiate between obscuration levels as those seen for the Swift/BAT AGNs. First, there may simply not be enough local redshift XXL-N AGNs for a proper statistical comparison to the results found for the Swift/BAT AGNs. Second, it is possible that the chosen redshift bins are not fine enough, and we are including AGNs across redshift ranges that are too large. After splitting the $z < 0.5$ bin into five sub-bins, however, we find the same result as before: the unobscured and heavily obscured AGNs coexist within the parameter space.

Another explanation lies in the reliability of the results of the X-ray spectral fitting performed in Liu et al. (2016). While the Bayesian statistical framework employed in that work is a powerful method for constraining the spectral properties for AGNs with low counts, our results suggest that the column densities derived for the AGNs may still be inaccurate due to the low counts acquired. For example, for all AGNs detected in the $z < 0.5$ bin, the median number of counts detected in the EPIC PN and two EPIC MOS detectors is only 16.8 and 15.1, respectively. Furthermore, identification of CT AGNs via XMM-Newton spectroscopy is quite difficult due to the softer X-ray passband (0.3–10 keV) probed with the XMM-Newton imaging. It can be very difficult to distinguish between the scenario in which the source is heavily obscured and the X-ray emission is dominated by reprocessed radiation from the circumnuclear material and that in which the source is unobscured but the emission is dominated by relativistic reflection from the accretion disk when using low signal-to-noise ratio X-ray spectra alone due to the strong model-dependent degeneracies involved (see, e.g., Gandhi et al. 2009; Treister et al. 2009). Our mid-IR ratio predictions for the highest X-ray column densities can hence be very complementary to help classify sources in which unobscured and obscured reflection models can fit an observed X-ray spectrum equally well.

Future, deeper XMM-Newton or NuSTAR follow-up observations could improve upon the current photon statistics and provide robust constraints on the column densities for at least the local XXL-N AGNs that lie within the diagnostic

[28] There are other moderately and heavily obscured WISE AGNs in this sample that did exhibit $\log(L_{\rm X}/L_{12\,\mu\rm m}) < -1.3$ but fall outside of our more stringent diagnostic region.

Table 7
Mid-IR AGNs from Kilerci Eser & Goto (2018) Selected via Equation (7)

AKARI ID	R.A.	Decl.	z	Selection Method	$\log\left(\frac{L_{22\,\mu m}}{L_{4.6\,\mu m}}\right)$	$\log\left(\frac{L_{X,\,Obs.}}{L_{12\,\mu m}}\right)$	Alternate ID	Obscuration Class	N_H Ref.
(1)	(2)	(3)	(4)	(5)	(6)	(7)	(8)	(9)	(10)
0041533+402120	10.473	40.355	0.071	3, 4	0.62	−1.52	Mrk 957	...	...
0138053–125210	24.522	−12.87	0.04	1, 2, 3, 4	0.47	−2.47	IRAS 01356–1307	Heavily obscured	1
0143576+022059	25.991	2.35	0.017	1, 2, 3, 4	0.35	−2.29	Mrk 573/UGC 1214	Heavily obscured	2
0150029–072549	27.511	−7.43	0.018	1, 2, 3, 4	0.64	−1.44	IRAS 01475–0740	Unobscured or heavily obscured	3, 4
0222435–084305	35.682	−8.719	0.045	1, 2, 3, 4	0.37	−1.72	NGC 905	...	...
0325256–060832	51.356	−6.144	0.034	4	0.36	−1.45	Mrk 609	Unobscured[a]	5
0330407–030814	52.670	−3.138	0.021	4	0.52	−1.73	Mrk 612	Moderately obscured	2
0452447–031256	73.186	−3.216	0.016	1, 2, 3, 4	0.64	−2.35	IRAS 04502–0317	...	...
0453257+040341	73.357	4.062	0.029	1, 2, 3, 4	0.18	−1.78	2MASX J04532576 +0403416	Moderately or heavily obscured	6, 7
0518178–344536	79.575	−34.761	0.066	4	0.49	−1.43	IRAS 05164–3448	...	...
0521013–252146	80.256	−25.363	0.043	1, 2, 3, 4	0.36	−1.44	IRAS 05189–2524	Lightly obscured[b]	7, 8
0525179–460023	81.325	−46.006	0.042	1, 2, 3, 4	0.42	−1.56	ESO 253-3	Moderately obscured	9
0742406+651031	115.674	65.177	0.037	1, 2, 3, 4	0.49	−1.58	Mrk 78	Heavily or moderately obscured	7, 10, 11
0759401+152314	119.917	15.387	0.016	4	0.41	−2.74	UGC 4145	...	...
0807411+390015	121.921	39.004	0.023	4	0.83	−2.04	Mrk 622	Heavily obscured	7
0810401+481233	122.668	48.209	0.077	3, 4	0.74	−2.11	2MASX J08104028 +4812335	Moderately obscured	1
0904011+012733	136.004	1.458	0.054	4	0.6	−2.54	IRAS 09014+0139	...	...
0935514+612112	143.965	61.353	0.039	1, 2, 3, 4	0.12	−2.28	UGC 5101	Heavily obscured	7, 12
1010432+061157	152.681	6.2	0.098	1, 2, 3, 4	0.57	−2.39	2MASS J10104334 +0612013	...	...
1021428+130655	155.428	13.115	0.076	4	0.92	−2.71	3XMM J102142.6 +130654	Unobscured	1, 13
1034080+600152	158.536	60.031	0.051	1, 2, 3, 4	0.47	−1.97	Mrk 34	Heavily obscured	14
1034381+393820	158.661	39.641	0.043	1, 2, 3, 4	0.15	−1.32	7C 103144.10 +395402.00	Unobscured	15
1100183+100255	165.075	10.049	0.036	3, 4	0.68	−2.28	LEDA 200263	Lightly obscured	16
1219585–355743	184.996	−35.960	0.058	1, 2, 3, 4	0.22	−2.74	6dFGS gJ121959.0–355735	...	...
1307059–234033	196.775	−23.677	0.01	4	0.55	−2.46	NGC 4968	Heavily obscured	17
1344421+555316	206.175	55.887	0.037	1, 2, 3, 4	0.89	−1.97	Mrk 273	Moderately obscured	8, 18
1347044+110626	206.768	11.106	0.023	1, 2, 3, 4	0.5	−1.81	Mrk 1361	...	...
1356027+182222	209.012	18.372	0.051	1, 2, 3, 4	0.17	−2.29	Mrk 463	Moderately obscured	19
1550415–035314	237.673	−3.888	0.03	1, 2, 3, 4	0.53	−1.97	IRAS 15480–0344	Heavily obscured	10, 18
1651053–012747	252.774	−1.463	0.041	4	0.38	−1.58	LEDA 1118057	...	...
1847441–630920	281.934	−63.157	0.015	3, 4	0.52	−2.43	IC 4769	Heavily obscured	10
1931212–723919	292.839	−72.656	0.062	1, 2, 3, 4	0.52	−2.23	Superantennae	Unobscured or heavily obscured	8, 20
2019593–523716	304.996	−52.622	0.017	4	0.34	−1.8	IC 4995	Moderately or heavily obscured	2, 10, 21
2059127–520024	314.804	−52.006	0.05	1, 2, 3, 4	0.33	−2.48	ESO 235-26	...	...
2316006+253326	349.003	25.557	0.027	1, 2, 3, 4	0.73	−2.23	IC 5298	Moderately obscured	22
2351135+201349	357.808	20.230	0.044	4	0.63	−1.37	MCG+03-60-031	...	...

Note. Column 1: AKARI ID from Kilerci Eser & Goto (2018). Columns 2–4: R.A., decl., and redshift of the AGN. Column 5: selection method satisfied by this AGN, where 1, 2, 3, and 4 correspond to the selection criteria in Stern et al. (2012), Jarrett et al. (2011), Assef et al. (2018), and Satyapal et al. (2018), respectively. Columns 6–7: $\log(L_{22\,\mu m}/L_{4.6\,\mu m})$ and $\log(L_{X,Obs.}/L_{12\,\mu m})$ luminosity ratios. Column 8: alternative identifier for candidate CT AGN from other literature studies. Column 9: obscuration class, assigned based on column density found in the literature. Class labels are adopted from Section 3. Column 9: reference(s) for column densities (used to classify the objects here): (1) Terashima et al. (2015), (2) Guainazzi et al. (2005), (3) Huang et al. (2011), (4) Brightman & Nandra (2008), (5) LaMassa et al. (2014), (6) Marchesi et al. (2018), (7) Ricci et al. (2017a), (8) Teng et al. (2015), (9) Asmus et al. (2015), (10) Severgnini et al. (2012), (11) Gilli et al. (2010), (12) Oda et al. (2017), (13) Teng & Veilleux (2010), (14) Gandhi et al. (2014), (15) González-Martín (2018), (16) Dutta et al. (2018), (17) LaMassa et al. (2019), (18) Brightman & Nandra (2011), (19) Bianchi et al. (2008), (20) Braito et al. (2009), (21) Noguchi et al. (2009), (22) Torres-Albà et al. (2018).

[a] Despite a lack of broad optical lines, Mrk 609 shows no sign of obscuration at X-ray wavelengths (LaMassa et al. 2014).

[b] Based upon current measurements, it is believed that IRAS 05189–2524 is currently lightly obscured, although it is possible that it may have been heavily obscured in the past (Teng et al. 2015).

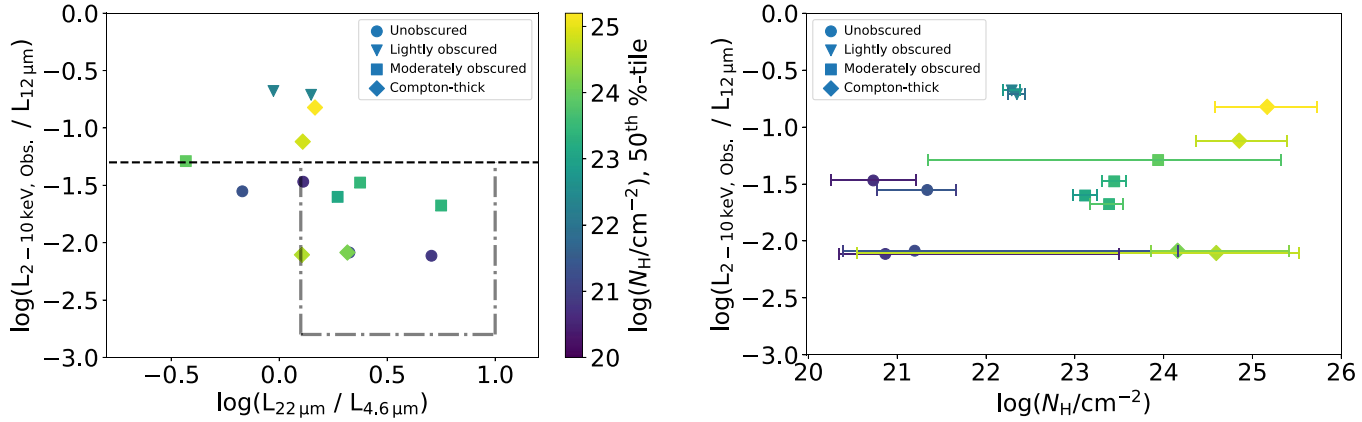

Figure 12. (Left) $L_{\mathrm{X,Obs.}}/L_{12\ \mu\mathrm{m}}$ vs. $L_{22\ \mu\mathrm{m}}/L_{4.6\ \mu\mathrm{m}}$ logarithmic ratios with each point color coded to indicate the 50th percentile $\log(N_{\mathrm{H}}/\mathrm{cm}^{-2})$ value. (Right) Logarithmic $L_{\mathrm{X,Obs.}}/L_{12\ \mu\mathrm{m}}$ ratio vs. $\log(N_{\mathrm{H}}/\mathrm{cm}^{-2})$, where the 50th percentile $\log(N_{\mathrm{H}}/\mathrm{cm}^{-2})$ and error values (16th and 84th percentiles) are drawn from Liu et al. (2016), and the data points are color coded according to the auxiliary axis to the left. To aid the reader, we use different markers to denote the obscuration bin for each source. Unlike the Swift/BAT AGNs, there is not as clear a relationship between the luminosity ratios and column density for the XXL-N AGNs, though this comparison should be viewed with caution because of the large uncertainties on $\log(N_{\mathrm{H}}/\mathrm{cm}^{-2})$ and because these AGNs were selected with a softer energy band (0.3–10 keV).

Table 8
Low-redshift Candidate Heavily Obscured AGNs from XMM XXL-N Selected via Equation (7)

UXID	α	δ	z	$F_{2-10\ \mathrm{keV}}$ (erg cm^{-2} s^{-1})	$\log(N_{\mathrm{H}}/\mathrm{cm}^{-2})$	$\log(L_{\mathrm{X,Obs.}}/L_{12\ \mu\mathrm{m}})$	$\log(L_{22\ \mu\mathrm{m}}/L_{4.6\ \mu\mathrm{m}})$
(1)	(2)	(3)	(4)	(5)	(6)	(7)	(8)
N_96_28	33.3335	−3.48755	0.0754	9.8×10^{-14}	$23.12^{+0.13}_{-0.14}$	−1.6	0.27
N_42_10	34.7902	−5.42083	0.0987	1.14×10^{-14}	$20.87^{+2.63}_{-0.52}$	−2.11	0.71
N_97_13	35.7049	−5.56736	0.0687	1.16×10^{-14}	$21.2^{+2.97}_{-0.8}$	−2.09	0.33
N_35_14	36.0105	−5.22831	0.0843	1.48×10^{-14}	$23.44^{+0.13}_{-0.13}$	−1.48	0.37
N_45_48	36.4573	−4.00696	0.0433	8.83×10^{-14}	$23.39^{+0.16}_{-0.21}$	−1.68	0.75
N_30_7	36.5185	−4.99197	0.0539	2.95×10^{-14}	$24.59^{+0.93}_{-4.05}$	−2.11	0.11
N_113_19	37.3037	−5.18955	0.0736	4.61×10^{-14}	$24.16^{+1.26}_{-0.3}$	−2.09	0.32
N_105_14	37.5322	−4.53268	0.0444	3.83×10^{-14}	$20.73^{+0.48}_{-0.48}$	−1.47	0.11

Note. All eight low-redshift ($z < 0.1$) candidate heavily obscured or CT AGNs within the XMM XXL-N field pulled from the Menzel et al. (2016) and Liu et al. (2016) catalogs selected using the diagnostic box defined by Equation (7). Column 1: unique X-ray identification string used by both Menzel et al. (2016) and Liu et al. (2016). Columns 2 and 3: X-ray source R.A. and decl. values (uncorrected for systematic offsets) given in degrees. Column 4: redshift. Column 5: hard X-ray 2–10 keV fluxes. Column 6: 50th percentile logarithmic line-of-sight column density derived by Liu et al. (2016). Error bounds are calculated using the 16th and 84th percentile column density values. Columns 7 and 8: values for the $\log(L_{\mathrm{X,Obs.}}/L_{12\ \mu\mathrm{m}})$ and $\log(L_{22\ \mu\mathrm{m}}/L_{4.6\ \mu\mathrm{m}})$ luminosity ratios.

boxes. For now, we identify these systems as candidate heavily obscured or CT AGNs, and we list their properties in Table 8.

5. Conclusions

Using the well-studied Swift/BAT sample of ultrahard X-ray–selected AGNs, we have presented an analysis of the AGN $L_{\mathrm{X,Obs.}}/L_{12\ \mu\mathrm{m}}$ luminosity ratio and two different mid-IR luminosity ratios, $L_{22\ \mu\mathrm{m}}/L_{4.6\ \mu\mathrm{m}}$ and $L_{12\ \mu\mathrm{m}}/L_{4.6\ \mu\mathrm{m}}$. Using the well-constrained X-ray (Ricci et al. 2017a) and mid-IR (Ichikawa et al. 2017) properties of the Swift/BAT AGNs, we probed the utility of these luminosity ratios as tools for inferring line-of-sight column densities and identifying the most heavily obscured AGNs in the local universe ($z < 0.1$). We summarize the results of our analysis as follows.

1. We have derived expressions relating the column density N_{H} to both the $L_{\mathrm{X,Obs.}}/L_{12\ \mu\mathrm{m}}$ and $L_{22\ \mu\mathrm{m}}/L_{4.6\ \mu\mathrm{m}}$ luminosity ratios, which are defined by Equations (2) and (4). These expressions can be inverted to give N_{H} as a function of the luminosity ratios. We provide these expressions again here:

$$\log(N_{\mathrm{H}}/\mathrm{cm}^{-2}) = 20 + (1.61^{+0.33}_{-0.31}) \times \log\left(\left|\frac{\log\left(\frac{L_{\mathrm{X,Obs.}}}{L_{12\ \mu\mathrm{m}}}\right) + (0.34^{+0.06}_{-0.06})}{(-0.003^{+0.002}_{-0.005})}\right|\right)$$

and

$$\log(N_{\mathrm{H}}/\mathrm{cm}^{-2}) = 20 + (3.86^{+1.94}_{-1.00}) \times \log\left(\left|\frac{\log\left(\frac{L_{22\ \mu\mathrm{m}}}{L_{4.6\ \mu\mathrm{m}}}\right) - (0.04^{+0.02}_{-0.02})}{(0.03^{+0.02}_{-0.02})}\right|\right).$$

2. We have demonstrated that unobscured and heavily obscured AGNs tend to exhibit different $L_{\mathrm{X,Obs.}}/L_{12\ \mu\mathrm{m}}$, $L_{22\ \mu\mathrm{m}}/L_{4.6\ \mu\mathrm{m}}$, and $L_{12\ \mu\mathrm{m}}/L_{4.6\ \mu\mathrm{m}}$ luminosity ratios. All

three of our diagnostic regions (Equations (5), (7), and (8)) identify (in general) the most heavily absorbed AGNs, with average column densities of $\log(N_{\rm H}/{\rm cm}^{-2}) \geqslant 24.0$ for each defined parameter space. These regions are all $\gtrsim$80% complete and $\gtrsim$60% pure for AGNs with $\log(N_{\rm H}/{\rm cm}^{-2}) \geqslant 24$. The greatest impurities arise due to AGNs with $23.5 \lesssim \log(N_{\rm H}/{\rm cm}^{-2}) < 24$; these regions are $\gtrsim$85% pure for AGNs with $\log(N_{\rm H}/{\rm cm}^{-2}) \gtrsim 23.5$.

3. While optically star-forming systems can fall within our diagnostic regions, this contamination can be virtually eliminated via mid-IR or X-ray selection criteria. Such selection criteria should be used judiciously to avoid removing non-mid-IR AGNs. These diagnostic regions should not be used to differentiate between AGNs and galaxies dominated by star formation.
4. Swift/BAT AGNs that do not dominate the total observed 12 μm emission tend to exhibit redder colors and larger X-ray deficits with increasing column density, suggesting that host galaxy contributions to at least the mid-IR emission can be a significant factor in the luminosity ratios examined here, particularly in the case of mildly obscured and CT AGNs selected with our diagnostics. However, it appears that this effect actually aids in the identification of CT AGNs, as the host contributions result in a larger separation in color space between less and more obscured AGNs.
5. We find that the selection criteria proposed here are more reliable at identifying obscured and CT AGNs than the mid- and far-IR selection criteria proposed by Kilerci Eser et al. (2020). We identify several known obscured and CT AGNs, as well as several candidate CT AGNs, within the IR galaxy catalog of Kilerci Eser & Goto (2018; see Table 7).
6. We applied our diagnostics to the XMM-Newton XXL-N field and found, in contrast to Swift/BAT AGNs, that obscured and unobscured XXL-N AGNs do not appear to exhibit distinctly different luminosity ratios. This disparity could be due to poor photon statistics or the softer X-ray energies probed for the XXL-N AGNs, which could lead to inaccurate column density values. Although, given the small number of $z < 0.1$ XXL-N AGNs and the large errors associated with several $N_{\rm H}$ values, this comparison should be viewed with caution.

Identifying heavily obscured AGNs remains an important yet difficult task, though the study of such AGNs is an important step in the development of our understanding of the evolution of AGNs. In a future study, we could expand our analysis to include diagnostic regions appropriately modified to differentiate between unobscured and heavily obscured sources at higher redshift, although it is difficult to speculate at the moment how the emission ratios may change with redshift, as both star formation and AGN activity are expected to increase with redshift.

The selection criteria presented here offer a complementary approach to the spectral curvature method developed in Koss et al. (2016), which is very effective at selecting heavily obscured AGNs at local z, with the caveats that one must already have hard X-ray (>10 keV) measurements with NuSTAR or Swift/BAT and that it is most effective for brighter AGNs. Softer X-ray missions can only be utilized for higher-redshift sources ($z \sim 3$) for which the hard X-ray emission has shifted into the rest-frame 10–30 keV passband

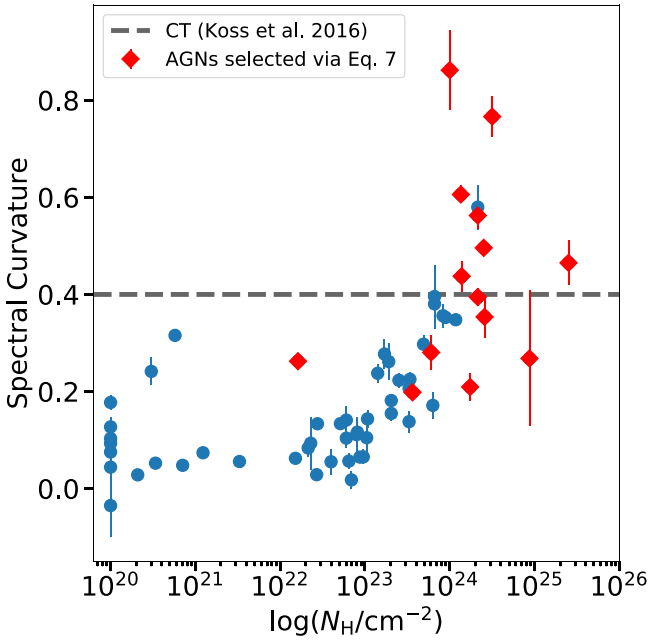

Figure 13. Comparison between the X-ray and mid-IR selection criteria introduced in this work and the spectral curvature method from Koss et al. (2016). The spectral curvature of each point was calculated using observations from NuSTAR, whereas the column densities come from Ricci et al. (2017a). Only AGNs with spectral curvature errors of <0.2 are included in this plot. The dashed gray line represents a spectral curvature value of 0.4, above which an AGN is considered to be CT. Red points are AGNs selected using the diagnostic box defined in Equation (7), whereas blue points are not selected via Equation (7). The spectral curvature method and the diagnostic defined in this work find several of the same sources. In fact, these two approaches also find CT AGNs missed by one another. A few CT AGNs fall below the 0.4 spectral curvature cutoff, yet the diagnostic presented here selects them; meanwhile, the spectral curvature method recovered a CT AGN missed by our new diagnostic. There is one outlier that is selected by Equation (7) and exhibits a relatively high spectral curvature, yet it possesses a column density of only $\sim 10^{22}$ cm^{-2}. This source, NGC 1365, is a well-known variable absorber and has gone through massive absorption transitions. Recent high signal-to-noise ratio observations have shown that the column density remains substantial, above 10^{23} cm^{-2} (e.g., Risaliti et al. 2009a, 2009b, 2009c; Maiolino et al. 2010; Walton et al. 2010; Brenneman et al. 2013), and occasionally increases to the extent of becoming CT (Risaliti et al. 2005). It is possible that the mid-IR emission is tracing a higher absorption period seen in past observations.

(Baronchelli et al. 2017). The diagnostics presented here, on the other hand, do not require higher-energy passbands in order to select local-z sources and can take advantage of softer X-ray missions such as Chandra and XMM-Newton. The synergy between these two approaches is best summed up by the fact that they select many of the same sources using different passbands and select heavily obscured AGNs missed by one another (Figure 13), yielding a more complete census of heavily obscured Swift/BAT AGNs overall.

The diagnostic regions proposed in this study, as well as the expressions derived relating $N_{\rm H}$ to the $L_{\rm X,Obs.}/L_{12\ \mu{\rm m}}$ and $L_{22\ \mu{\rm m}}/L_{4.6\ \mu{\rm m}}$ luminosity ratios, could be used to differentiate between unobscured and heavily obscured AGNs in future large samples of AGNs, such as those now being detected by the eROSITA all-sky survey (Predehl et al. 2010; Merloni et al. 2012). In particular, the eROSITA survey will provide the first all-sky X-ray imaging survey at energies up to 10 keV, yielding a highly complementary catalog to those of other all-sky missions, such as WISE. Future works could cross-match the WISE and eROSITA catalogs and use the diagnostics presented

here to identify many more cases of CT AGN candidates, select targets for deeper follow-up multiwavelength observations, and compute the CT fraction for the future sample, all of which will be crucial in the quest to construct a more complete census of CT AGNs and gain a better understanding of obscured AGNs.

We graciously thank the anonymous referee whose timely and constructive feedback aided in improving this work. We thank L. Shao and R. Boissay-Malaquin for their helpful comments on the draft. R.W.P. thanks B. L. Cale for helpful discussions regarding data fitting with Python. C.R. acknowledges support from the Fondecyt Iniciacion grant 11190831 and ANID BASAL project FB210003. P.G.B. acknowledges financial support from the STFC and Czech Science Foundation project No. 19-05599Y. D.A. acknowledges funding through the European Union's Horizon 2020 innovation program under Marie Sklodowska-Curie grant agreement No. 793499 (DUSTDEVILS). B.T. acknowledges support from the Israel Science Foundation (grant 1849/19) and from the European Research Council (ERC) under the European Union's Horizon 2020 research and innovation program (grant agreement 950533). M.K. acknowledges support from NASA through ADAP award NNH16CT03C. F.R. acknowledges support from FONDECYT postdoctorado 3180506. E.T. acknowledges support from FONDECYT Regular 1190818 and 1200495, ANID grants CATA-Basal AFB-170002, ACE210002, and FB210003, and Millennium Nucleus NCN19_058. This work is partially supported by the Japan Society for the Promotion of Science (JSPS) KAKENHI (18K13584 and 20H01939; K.I.). K.O. acknowledges support from the National Research Foundation of Korea (NRF-2020R1C1C1005462). M.S. acknowledges support by the Ministry of Education, Science and Technological Development of the Republic of Serbia through contract No. 451-03-68/2020/14/20002 and the Science Fund of the Republic of Serbia, PROMIS 6060916, BOWIE.

Facilities: Chandra, GALEX, NuSTAR, SDSS, Suzaku, Swift, WISE, XMM-Newton.

Software: odr (Boggs & Rogers et al. 1990; Virtanen et al. 2020), pandas (McKinney 2010), scipy (Virtanen et al. 2020), numpy (Oliphant 2006; van der Walt et al. 2011; Oliphant 2015), matplotlib (Hunter 2007), BXA (Buchner et al. 2014).

This publication makes use of data products from the Wide-field Infrared Survey Explorer, which is a joint project of the University of California, Los Angeles, and the Jet Propulsion Laboratory/California Institute of Technology, funded by the National Aeronautics and Space Administration. Funding for SDSS-III has been provided by the Alfred P. Sloan Foundation, the Participating Institutions, the National Science Foundation, and the U.S. Department of Energy Office of Science. The SDSS-III website is http://www.sdss3.org/.

This research has made use of the NASA/IPAC Extragalactic Database (NED), which is operated by the Jet Propulsion Laboratory, California Institute of Technology, under contract with the National Aeronautics and Space Administration.

Appendix

A.1. Exploring the Origin of the Scatter in the $L_{22\ \mu m}/L_{4.6\ \mu m}$ versus N_H Correlation

In the process of our analysis, we explored whether any quality or selection cuts could be applied to the data to reduce the scatter observed in panel (a) of Figures 3 and 4. Our parent sample was divided into four subsamples as shown in Figure 14:

1. AGN-dominated systems with W1 − W2 > 0.8 (Stern et al. 2012; blue squares);
2. AGNs not selected using the aforementioned WISE cut, i.e., W1 − W2 < 0.8 (red triangles);
3. AGNs with >300 spectral counts in the X-ray spectra, which provides a statistically significant number of counts to constrain $N_{\rm H}$ in the X-ray spectral fitting analysis (Ricci et al. 2017a; cyan inverted triangles); and
4. AGNs with observed 2–10 keV luminosities in excess of 10^{42} erg s^{-1} (green diamonds).

In Figures 14 and 15, we compare these subsamples for the $L_{22\ \mu m}/L_{4.6\ \mu m}$ and $L_{12\ \mu m}/L_{4.6\ \mu m}$ luminosity ratios, respectively, and how they correlate with $N_{\rm H}$. The resulting mean values per bin for each different subsample are consistent with the values (the error bars represent the standard deviation of each subsample) originally found for the parent sample; interestingly, the observed correlation between WISE color and column density holds for AGNs that satisfy the Stern et al. (2012) criterion, as well as AGNs that do not satisfy that criterion. We observe a larger difference in the $L_{22\ \mu m}/L_{4.6\ \mu m}$ ratios when moving to higher column densities than for the $L_{12\ \mu m}/L_{4.6\ \mu m}$ ratios. Additionally, as shown in Figure 4, while there is a large amount of scatter in the lowest $N_{\rm H}$ bin of the bottom panel of Figure 15, this scatter is likely due to the low number of sources within that bin, and this still does not overlap the bin probing the highest obscuring columns. Due to the consistency between the results for the subsamples and that found for the parent sample, we do not implement any of these cuts during our analysis.

From Figures 14 and 15, it becomes clear that there a number of WISE AGNs (W1 − W2 > 0.8) within the Swift/BAT sample that exhibit extremely red mid-IR colors with $\log(L_{22\ \mu m}/L_{4.6\ \mu m}) > 0.5$, suggesting significant obscuration. We tabulate these WISE AGNs in Table 9. Indeed, the majority of these AGNs (18/23) are moderately to heavily obscured with $\log(N_{\rm H}/{\rm cm}^{-2}) > 23$, though there are a few exceptions, notably

1. HS 0328+0528, an unobscured Seyfert 1;
2. IRAS 05189–2524, a lightly obscured Seyfert 2;
3. 2MASX J09172716–6456271, an unobscured Seyfert 2;
4. MCG-1-24-12, a lightly obscured Seyfert 2; and
5. NGC 4253, an unobscured Seyfert 1.

The WISE selection based on the cut defined in Stern et al. (2012) is not, however, necessarily a good method for selecting obscured over unobscured AGNs. As we discussed in Section 4.3, 40/71 of AGNs with $\log(N_{\rm H}/{\rm cm}^{-2}) > 5.0 \times 10^{23}$ cm^{-2} in the Swift/BAT sample studied here do not meet a color cut of W1 − W2 > 0.8, reinforcing our choice to not invoke such a cut on the parent sample.

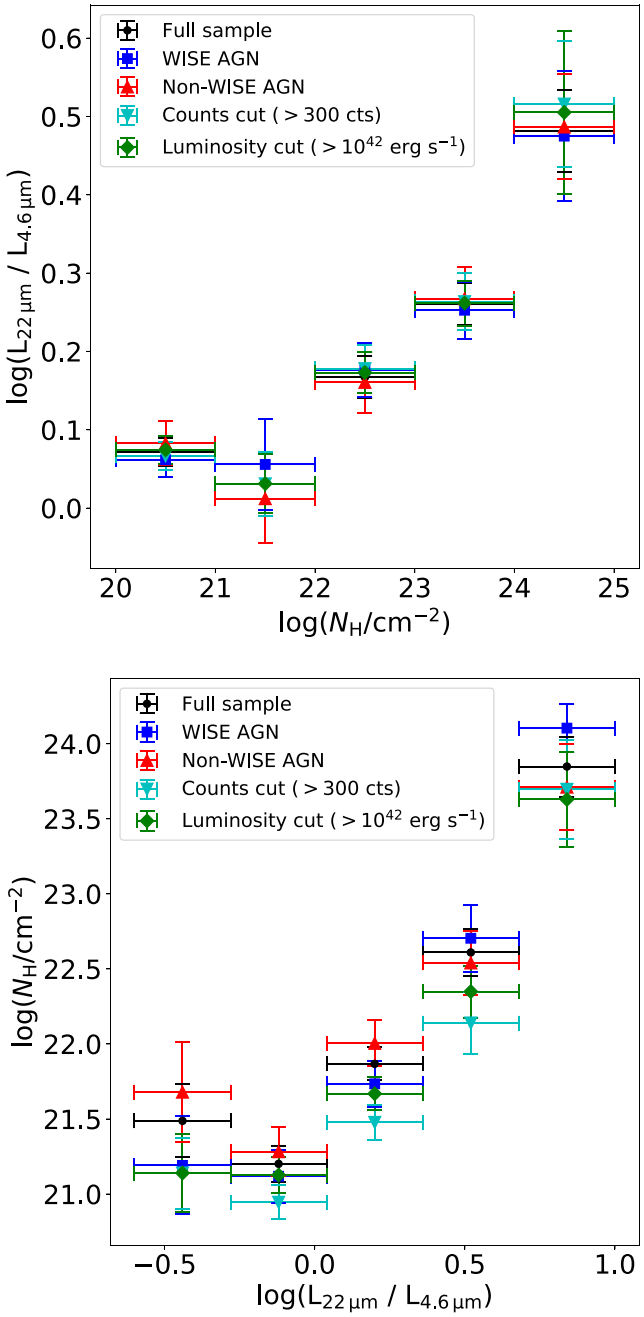

Figure 14. We applied four different cuts to our full Swift/BAT sample to explore the origin of the scatter observed in Figure 3. Here we present two different comparisons of the derived values for $N_{\rm H}$ from Ricci et al. (2017a) and the $L_{22\ \mu m}/L_{4.6\ \mu m}$ mid-IR ratios, where we have (top panel) binned by $\log(N_{\rm H})$ and (bottom panel) binned by the $L_{22\ \mu m}/L_{4.6\ \mu m}$ ratio. We observe more scatter when binning by the mid-IR ratio than we do when binning by $N_{\rm H}$, but nonetheless, the general trend is the same: we observe increasing mid-IR ratios of $L_{22\ \mu m}/L_{4.6\ \mu m}$ with increasing column density regardless of the subsample.

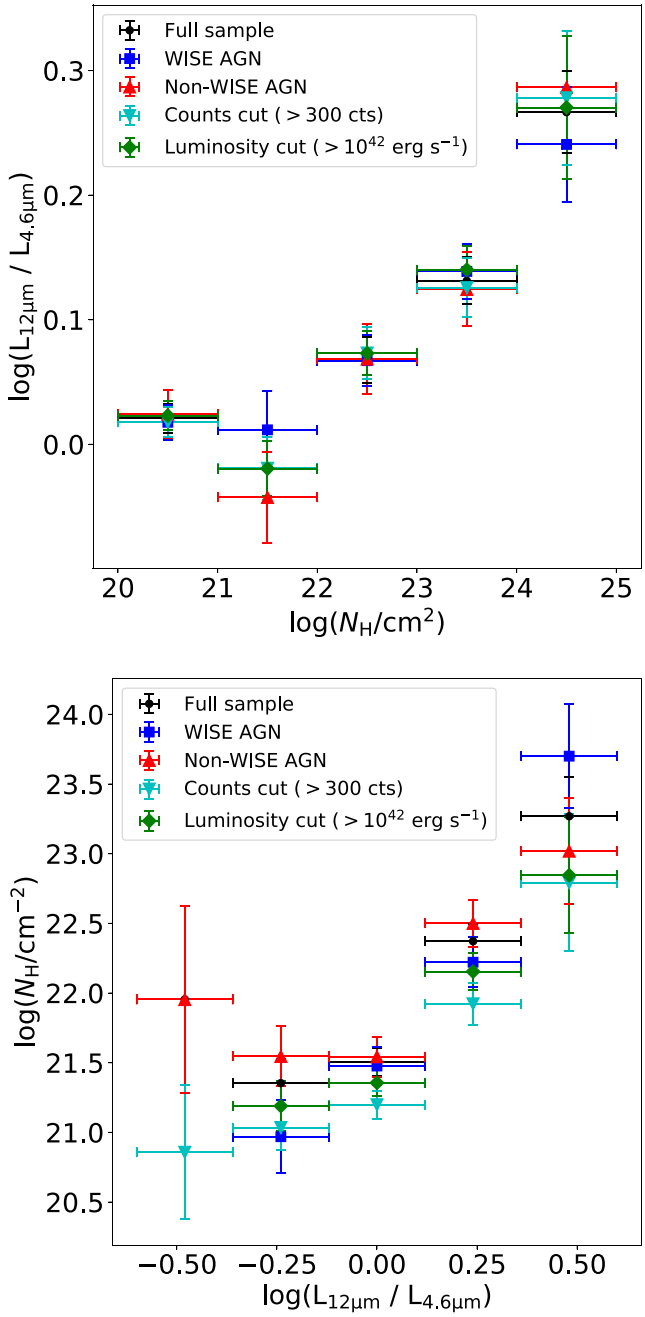

Figure 15. Analogous to Figure 14, except here we examine the alternative mid-IR diagnostic ratio that depends upon $L_{12\ \mu m}$ and $L_{4.6\ \mu m}$. We observe an increase in the mid-IR ratio of $L_{12\ \mu m}/L_{4.6\ \mu m}$ with column density, as was observed with $L_{22\ \mu m}/L_{4.6\ \mu m}$, although with a large amount of scatter in the $N_{\rm H}$ values for the lowest mid-IR ratio bin. However, given that our focus is on the most heavily obscured sources (>a few times 10^{23} cm^{-2}), this scatter is not a concern.

Table 9
WISE-selected Swift/BAT AGNs with $\log(L_{22\ \mu m}/L_{4.6\ \mu m}) > 0.5$

SWIFT ID (1)	R.A. (2)	Decl. (3)	z (4)	$\log\left(\frac{L_{22\ \mu m}}{L_{4.6\ \mu m}}\right)$ (5)	$\log\left(\frac{L_{X,\ Obs.}}{L_{12\ \mu m}}\right)$ (6)	Alternate ID (7)	$\log(N_H/cm^{-2})$ (8)
SWIFT J0107.7–1137B	16.9152	−11.65320	0.0475	0.51	−1.10	2MASX J01073963–1139117	$23.58^{+0.28}_{-0.18}$
SWIFT J0122.8+5003	20.6435	50.05500	0.0204	0.76	−1.44	MCG+8-3-18	$24.24^{+0.34}_{-0.15}$
SWIFT J0308.2–2258	47.0449	−22.96080	0.0360	0.89	−1.78	NGC 1229	$24.94^{+1.06}_{-0.45}$
SWIFT J0331.3+0538	52.7174	5.64040	0.0460	0.62	−0.35	HS 0328+0528	$20.00^{+0.00}_{-0.00}$
SWIFT J0521.0–2522	80.2561	−25.36260	0.0426	0.51	−1.74	IRAS 05189–2524	$22.92^{+0.04}_{-0.03}$
SWIFT J0615.8+7101	93.9015	71.03750	0.0135	0.82	−1.20	Mrk 3	$24.07^{+0.06}_{-0.04}$
SWIFT J0656.4–4921	104.0498	−49.33060	0.0410	0.58	−1.79	LEDA 478026	$24.03^{+0.30}_{-0.10}$
SWIFT J0743.0+6513	115.6739	65.17710	0.0371	0.66	−1.82	Mrk 78	$24.11^{+0.08}_{-0.12}$
SWIFT J0804.2+0507	121.0244	5.11380	0.0135	0.77	−1.09	Mrk 1210	$23.40^{+0.06}_{-0.08}$
SWIFT J0843.5+3551	130.9375	35.82830	0.0540	0.58	−1.09	CASG 218	$23.61^{+0.24}_{-0.21}$
SWIFT J0917.2–6457	139.3634	−64.94090	0.0860	0.55	−0.07	2MASX J09172716–6456271	$21.41^{+0.33}_{-0.71}$
SWIFT J0920.8–0805	140.1927	−8.05610	0.0196	0.54	−0.28	MCG-1-24-12	$22.81^{+0.05}_{-0.03}$
SWIFT J1214.3+2933	183.5741	29.52860	0.0632	0.53	−0.94	Was 49b	$23.41^{+0.17}_{-0.11}$
SWIFT J1218.5+2952	184.6105	29.81290	0.0129	0.56	−0.81	NGC 4253	$20.32^{+0.08}_{-0.17}$
SWIFT J1225.8+1240	186.4448	12.66210	0.0084	0.61	−0.77	NGC 4388	$23.52^{+0.02}_{-0.01}$
SWIFT J1238.6+0928	189.6810	9.46017	0.0829	0.64	−0.93	SDSS J123843.43+092736.6	$23.60^{+0.09}_{-0.07}$
SWIFT J1322.2–1641	200.6019	−16.72860	0.0165	0.63	−1.86	MCG-3-34-64	$23.80^{+0.02}_{-0.02}$
SWIFT J1717.1–6249	259.2478	−62.82060	0.0037	0.51	−1.16	NGC 6300	$23.31^{+0.02}_{-0.03}$
SWIFT J1800.3+6637	270.0304	66.61510	0.0265	0.94	−1.62	NGC 6552	$24.05^{+0.35}_{-0.22}$
SWIFT J2052.0–5704	313.0098	−57.06880	0.0114	0.73	−1.45	IC 5063	$23.56^{+0.07}_{-0.01}$
SWIFT J2207.3+1013	331.7582	10.23340	0.0267	0.71	−1.70	UGC 11910	$24.41^{+0.07}_{-0.07}$
SWIFT J2304.9+1220	346.2361	12.32290	0.0079	0.82	−2.65	NGC 7479	$24.16^{+0.12}_{-0.13}$
SWIFT J2343.9+0537	355.9982	5.64000	0.0560	0.52	−0.62	LEDA 3092070	$23.26^{+0.19}_{-0.08}$

Note. WISE-selected Swift/BAT AGNs (W1 − W2 > 0.8; Stern et al. 2012) that exhibit mid-IR ratios of $\log(L_{22\ \mu m}/L_{4.6\ \mu m}) > 0.5$. Column 1: SWIFT ID number. Columns 2–4: R.A., decl., and redshift. Columns 5 and 6: $\log(L_{X,Obs.}/L_{12\ \mu m})$ and $\log(L_{22\ \mu m}/L_{4.6\ \mu m})$ luminosity ratios. Column 7: alternative ID drawn from Ricci et al. (2017a). Column 8: column density derived in Ricci et al. (2017a).

ORCID iDs

Ryan W. Pfeifle https://orcid.org/0000-0001-8640-8522
Claudio Ricci https://orcid.org/0000-0001-5231-2645
Peter G. Boorman https://orcid.org/0000-0001-9379-4716
Marko Stalevski https://orcid.org/0000-0001-5146-8330
Daniel Asmus https://orcid.org/0000-0003-0220-2063
Benny Trakhtenbrot https://orcid.org/0000-0002-3683-7297
Michael J. Koss https://orcid.org/0000-0002-7998-9581
Daniel Stern https://orcid.org/0000-0003-2686-9241
Federica Ricci https://orcid.org/0000-0001-5742-5980
Shobita Satyapal https://orcid.org/0000-0003-2277-2354
Kohei Ichikawa https://orcid.org/0000-0002-4377-903X
David J. Rosario https://orcid.org/0000-0002-0001-3587
Turgay Caglar https://orcid.org/0000-0002-9144-2255
Ezequiel Treister https://orcid.org/0000-0001-7568-6412
Meredith Powell https://orcid.org/0000-0003-2284-8603
Kyuseok Oh https://orcid.org/0000-0002-5037-951X
C. Megan Urry https://orcid.org/0000-0002-0745-9792

References

Aihara, H., Allende Prieto, C., An, D., et al. 2011, ApJS, 193, 29
Akylas, A., Georgakakis, A., Georgantopoulos, I., Brightman, M., & Nandra, K. 2012, A&A, 546, A98
Alexander, D. M., Chary, R. R., Pope, A., et al. 2008, ApJ, 687, 835
Alexander, D. M., & Hickox, R. C. 2012, NewAR, 56, 93
Ananna, T. T., Treister, E., Urry, C. M., et al. 2019, ApJ, 871, 240
Antonucci, R. 1993, ARA&A, 31, 473
Asmus, D., Gandhi, P., Hönig, S. F., Smette, A., & Duschl, W. J. 2015, MNRAS, 454, 766
Asmus, D., Hönig, S. F., & Gandhi, P. 2016, ApJ, 822, 109
Assef, R. J., Stern, D., Noirot, G., et al. 2018, ApJS, 234, 23
Baldwin, J. A., Phillips, M. M., & Terlevich, R. 1981, PASP, 93, 5
Baron, D., & Netzer, H. 2019a, MNRAS, 482, 3915
Baron, D., & Netzer, H. 2019b, MNRAS, 486, 4290
Baronchelli, L., Koss, M., Schawinski, K., et al. 2017, MNRAS, 471, 364
Bauer, F. E., Arévalo, P., Walton, D. J., et al. 2015, ApJ, 812, 116
Baumgartner, W. H., Tueller, J., Markwardt, C. B., et al. 2013, ApJS, 207, 19
Bianchi, S., Chiaberge, M., Piconcelli, E., Guainazzi, M., & Matt, G. 2008, MNRAS, 386, 105
Blecha, L., Snyder, G. F., Satyapal, S., & Ellison, S. L. 2018, MNRAS, 478, 3056
Braito, V., Reeves, J. N., Della Ceca, R., et al. 2009, A&A, 504, 53
Brenneman, L. W., Risaliti, G., Elvis, M., & Nardini, E. 2013, MNRAS, 429, 2662
Brightman, M., & Nandra, K. 2008, MNRAS, 390, 1241
Brightman, M., & Nandra, K. 2011, MNRAS, 413, 1206
Boggs, P. T., & Rogers, J. E. 1990, in Proc. of the AMS-IMS-SIAM Joint Summer Research Conf., ed. P. J. Brown & W. A. Fuller (Providence, RI: American Mathematical Society), 183
Buchner, J., Georgakakis, A., Nandra, K., et al. 2014, A&A, 564, A125
Buchner, J., Georgakakis, A., Nandra, K., et al. 2015, ApJ, 802, 89
Burlon, D., Ajello, M., Greiner, J., et al. 2011, ApJ, 728, 58
Cameron, E. 2011, PASA, 28, 128
Carroll, C. M., Hickox, R. C., Ananna, T. T., et al. 2022, ApJ, submitted
Carroll, C. M., Hickox, R. C., Masini, A., et al. 2021, ApJ, 908, 185
Dutta, R., Srianand, R., & Gupta, N. 2018, MNRAS, 480, 947
Elvis, M., Maccacaro, T., Wilson, A. S., et al. 1978, MNRAS, 183, 129
Fabian, A. C., Zoghbi, A., Ross, R. R., et al. 2009, Natur, 459, 540
Ferland, G. J., Chatzikos, M., Guzmán, F., et al. 2017, RMxAA, 53, 385
Ferland, G. J., Porter, R. L., van Hoof, P. A. M., et al. 2013, RMxAA, 49, 137
Ferrarese, L., & Merritt, D. 2000, ApJL, 539, L9

Gandhi, P., Horst, H., Smette, A., et al. 2009, A&A, 502, 457
Gandhi, P., Lansbury, G. B., Alexander, D. M., et al. 2014, ApJ, 792, 117
Georgantopoulos, I., Rovilos, E., Akylas, A., et al. 2011, A&A, 534, A23
Gilli, R., Comastri, A., & Hasinger, G. 2007, A&A, 463, 79
Gilli, R., Vignali, C., Mignoli, M., et al. 2010, A&A, 519, A92
Gonzalez-Delgado, R. M., Perez, E., Diaz, A. I., et al. 1995, ApJ, 439, 604
González-Martín, O. 2018, ApJ, 858, 2
Goulding, A. D., Alexander, D. M., Mullaney, J. R., et al. 2011, MNRAS, 411, 1231
Guainazzi, M., Matt, G., & Perola, G. C. 2005, A&A, 444, 119
Haardt, F., & Maraschi, L. 1991, ApJL, 380, L51
Haardt, F., & Maraschi, L. 1993, ApJ, 413, 507
Herrero-Illana, R., Pérez-Torres, M. Á., Alonso-Herrero, A., et al. 2014, ApJ, 786, 156
Hönig, S. F. 2019, ApJ, 884, 171
Hönig, S. F., & Kishimoto, M. 2010, A&A, 523, A27
Hönig, S. F., & Kishimoto, M. 2017, ApJL, 838, L20
Hönig, S. F., Kishimoto, M., Antonucci, R., et al. 2012, ApJ, 755, 149
Hönig, S. F., Kishimoto, M., Tristram, K. R. W., et al. 2013, ApJ, 771, 87
Hopkins, P. F., Cox, T. J., Kereš, D., & Hernquist, L. 2008, ApJS, 175, 390
Huang, X.-X., Wang, J.-X., Tan, Y., Yang, H., & Huang, Y.-F. 2011, ApJL, 734, L16
Hunter, J. D. 2007, CSE, 9, 90
Ichikawa, K., Ricci, C., Ueda, Y., et al. 2017, ApJ, 835, 74
Ichikawa, K., Ricci, C., Ueda, Y., et al. 2019, ApJ, 870, 31
Ichikawa, K., Ueda, Y., Terashima, Y., et al. 2012, ApJ, 754, 45
Jarrett, T. H., Cohen, M., Masci, F., et al. 2011, ApJ, 735, 112
Kalberla, P. M. W., Burton, W. B., Hartmann, D., et al. 2005, A&A, 440, 775
Kilerci Eser, E., & Goto, T. 2018, MNRAS, 474, 5363
Kilerci Eser, E., Goto, T., Guver, T., Tuncer, A., & Atas, O. H. 2020, MNRAS, 494, 5793
Kocevski, D. D., Brightman, M., Nandra, K., et al. 2015, ApJ, 814, 104
Kormendy, J., & Ho, L. C. 2013, ARA&A, 51, 511
Koss, M., Trakhtenbrot, B., Ricci, C., et al. 2017, ApJ, 850, 74
Koss, M. J., Assef, R., Baloković, M., et al. 2016, ApJ, 825, 85
Koss, M. J., Ricci, C., Trakhtenbrot, B., et al. 2022, ApJS, 261, 2
LaMassa, S. M., Yaqoob, T., Boorman, P. G., et al. 2019, ApJ, 887, 173
LaMassa, S. M., Yaqoob, T., Ptak, A. F., et al. 2014, ApJ, 787, 61
Lamperti, I., Koss, M., Trakhtenbrot, B., et al. 2017, MNRAS, 467, 540
Lansbury, G. B., Alexander, D. M., Del Moro, A., et al. 2014, ApJ, 785, 17
Lansbury, G. B., Gandhi, P., Alexander, D. M., et al. 2015, ApJ, 809, 115
Laor, A., & Draine, B. T. 1993, ApJ, 402, 441
Levenson, N. A., Radomski, J. T., Packham, C., et al. 2009, ApJ, 703, 390
Li, A., & Draine, B. T. 2001, ApJ, 554, 778
Liu, Z., Merloni, A., Georgakakis, A., et al. 2016, MNRAS, 459, 1602
Lutz, D., Maiolino, R., Spoon, H. W. W., & Moorwood, A. F. M. 2004, A&A, 418, 465
Maiolino, R., Risaliti, G., Salvati, M., et al. 2010, A&A, 517, A47
Marchesi, S., Ajello, M., Marcotulli, L., et al. 2018, ApJ, 854, 49
Mateos, S., Carrera, F. J., Alonso-Herrero, A., et al. 2015, MNRAS, 449, 1422
Mathis, J. S., Rumpl, W., & Nordsieck, K. H. 1977, ApJ, 217, 425
McKinney, W. 2010, in Proc. 9th Python in Science Conf., ed. S. van der Walt & J. Millman, 51
Menzel, M. L., Merloni, A., Georgakakis, A., et al. 2016, MNRAS, 457, 110
Merloni, A., Predehl, P., Becker, W., et al. 2012, arXiv:1209.3114
Netzer, H. 2015, ARA&A, 53, 365
Noguchi, K., Terashima, Y., & Awaki, H. 2009, ApJ, 705, 454
Oda, S., Tanimoto, A., Ueda, Y., et al. 2017, ApJ, 835, 179
Oh, K., Koss, M., Markwardt, C. B., et al. 2018, ApJS, 235, 4
Oh, K., Koss, M. J., Ueda, Y., et al. 2022, ApJS, 261, 4
Oliphant, T. E. 2006, A Guide to NumPy, Vol. 1 (USA: Trelgol Publishing)
Oliphant, T. E. 2015, Guide to NumPy (2nd ed.; North Charleston, SC: CreateSpace Independent Publishing Platform)
Pereira-Santaella, M., Alonso-Herrero, A., Santos-Lleo, M., et al. 2011, A&A, 535, A93
Pfeifle, R. W., Satyapal, S., Secrest, N. J., et al. 2019, ApJ, 875, 117
Pierre, M., Adami, C., Birkinshaw, M., et al. 2017, AN, 338, 334
Pierre, M., Pacaud, F., Adami, C., et al. 2016, A&A, 592, A1
Predehl, P., Böhringer, H., Brunner, H., et al. 2010, in AIP Conf. Proc. 1248, X-ray Astronomy 2009; Present Status, Multi-Wavelength Approach and Future Perspectives, ed. A. Comastri, L. Angelini, & M. Cappi (Melville, NY: AIP), 543
Predehl, P., & Schmitt, J. H. M. M. 1995, A&A, 500, 459
Puccetti, S., Comastri, A., Bauer, F. E., et al. 2016, A&A, 585, A157
Ramos Almeida, C., & Ricci, C. 2017, NatAs, 1, 679
Ricci, C., Bauer, F. E., Treister, E., et al. 2017b, MNRAS, 468, 1273
Ricci, C., Ueda, Y., Koss, M. J., et al. 2015, ApJL, 815, L13
Ricci, C., Trakhtenbrot, B., Koss, M. J., et al. 2017a, ApJS, 233, 17
Risaliti, G., Braito, V., Laparola, V., et al. 2009c, ApJL, 705, L1
Risaliti, G., Elvis, M., Fabbiano, G., Baldi, A., & Zezas, A. 2005, ApJL, 623, L93
Risaliti, G., Miniutti, G., Elvis, M., et al. 2009a, ApJ, 696, 160
Risaliti, G., Salvati, M., Elvis, M., et al. 2009b, MNRAS, 393, L1
Rovilos, E., Georgantopoulos, I., Akylas, A., et al. 2014, MNRAS, 438, 494
Sakamoto, K., Aalto, S., Costagliola, F., et al. 2013, ApJ, 764, 42
Satyapal, S., Abel, N. P., & Secrest, N. J. 2018, ApJ, 858, 38
Severgnini, P., Caccianiga, A., & Della Ceca, R. 2012, A&A, 542, A46
Smith, B. J., Struck, C., & Nowak, M. A. 2005, AJ, 129, 1350
Stalevski, M., Asmus, D., & Tristram, K. R. W. 2018, POBeo, 98, 203
Stalevski, M., Fritz, J., Baes, M., Nakos, T., & Popović, L. Č. 2012, MNRAS, 420, 2756
Stalevski, M., Ricci, C., Ueda, Y., et al. 2016, MNRAS, 458, 2288
Stern, D., Assef, R. J., Benford, D. J., et al. 2012, ApJ, 753, 30
Teng, S. H., Rigby, J. R., Stern, D., et al. 2015, ApJ, 814, 56
Teng, S. H., & Veilleux, S. 2010, ApJ, 725, 1848
Terashima, Y., Hirata, Y., Awaki, H., et al. 2015, ApJ, 814, 11
Toba, Y., Yamada, S., Ueda, Y., et al. 2020, ApJ, 888, 8
Torres-Albà, N., Iwasawa, K., Díaz-Santos, T., et al. 2018, A&A, 620 A140
Treister, E., Urry, C. M., & Virani, S. 2009, ApJ, 696, 110
Tristram, K. R. W., Burtscher, L., Jaffe, W., et al. 2014, A&A, 563, A82
Ueda, Y., Akiyama, M., Hasinger, G., Miyaji, T., & Watson, M. G. 2014, ApJ, 786, 104
Urry, C. M., & Padovani, P. 1995, PASP, 107, 803
van der Walt, S., Colbert, S. C., & Varoquaux, G. 2011, CSE, 13, 22
Virtanen, P., Gommers, R., Oliphant, T. E., et al. 2020, NatMe, 17, 261
Walton, D. J., Reis, R. C., & Fabian, A. C. 2010, MNRAS, 408, 601
Webb, N. A., Coriat, M., Traulsen, I., et al. 2020, A&A, 641, A136
Xu, C. K., Cao, C., Lu, N., et al. 2015, ApJ, 799, 11
Yan, W., Hickox, R. C., Hainline, K. N., et al. 2019, ApJ, 870, 33